Atmos. Chem. Phys. Discuss., 15, 12007–12067, 2015
www.atmos-chem-phys-discuss.net/15/12007/2015/
doi:10.5194/acpd-15-12007-2015

Atmospheric Chemistry and Physics Discussions

How consistent are top-down hydrocarbon emissions based on formaldehyde observations from GOME-2 and OMI?

T. Stavrakou[1], J.-F. Müller[1], M. Bauwens[1], I. De Smedt[1], M. Van Roozendael[1], M. De Mazière[1], C. Vigouroux[1], F. Hendrick[1], M. George[2], C. Clerbaux[2,3], P.-F. Coheur[3], and A. Guenther[4]

[1]Belgian Institute for Space Aeronomy, Avenue Circulaire 3, 1180, Brussels, Belgium
[2]UPMC Univ. Paris 6; Université Versailles St.-Quentin; CNRS/INSU, LATMOS-IPSL, 75252, CEDEX 05, Paris, France
[3]Spectroscopie de l'Atmosphère, Service de Chimie Quantique et Photophysique, Université Libre de Bruxelles, 1050, Belgium
[4]Atmospheric Sciences and Global Change Division, Pacific Northwest National Laboratory, Richland, WA, USA

Received: 19 March 2015 – Accepted: 9 April 2015 – Published: 22 April 2015

Correspondence to: T. Stavrakou (jenny@aeronomie.be)

Published by Copernicus Publications on behalf of the European Geosciences Union.

ACPD
15, 12007–12067, 2015

Abstract

The vertical columns of formaldehyde (HCHO) retrieved from two satellite instruments, the Global Ozone Monitoring Instrument-2 (GOME-2) on Metop-A and the Ozone Monitoring Instrument (OMI) on Aura, are used to constrain global emissions of HCHO precursors from open fires, vegetation and human activities in the year 2010. To this end, the emissions are varied and optimized using the adjoint model technique in the IMAGESv2 global CTM (chemistry-transport model) on a monthly basis and at the model resolution. Given the different local overpass times of GOME-2 (09:30 LT) and OMI (13:30 LT), the simulated diurnal cycle of HCHO columns is investigated and evaluated against ground-based optical measurements at 7 sites in Europe, China and Africa. The modelled diurnal cycle exhibits large variability, reflecting competition between photochemistry and emission variations, with noon or early afternoon maxima at remote locations (oceans) and in regions dominated by anthropogenic emissions, late afternoon or evening maxima over fire scenes, and midday minima in isoprene-rich regions. The agreement between simulated and ground-based columns is found to be generally better in summer (with a clear afternoon maximum at mid-latitude sites) than in winter, and the annually averaged ratio of afternoon to morning columns is slightly higher in the model (1.126) than in the ground-based measurements (1.043).

The anthropogenic VOC (volatile organic compound) sources are found to be weakly constrained by the inversions on the global scale, mainly owing to their generally minor contribution to the HCHO columns, except over strongly polluted regions, like China. The OMI-based inversion yields total flux estimates over China close to the bottom-up inventory (24.6 vs. 25.5 in the a priori) with, however, pronounced increases in the Northeast China and reductions in the south. Lower fluxes are estimated based on GOME-2 HCHO columns (20.6 TgVOC), in particular over the Northeast, likely reflecting mismatches between the observed and the modelled diurnal cycle in this region.

The resulting biogenic and pyrogenic flux estimates from both optimizations generally show a good degree of consistency. A reduction of the global annual biogenic

ACPD
15, 12007–12067, 2015

emissions of isoprene is derived, by 9 and by 13 % according to GOME-2 and OMI, respectively, compared to the a priori estimate of 363 Tg in 2010. The reduction is largest (up to 25–40 %) in the Southeastern US, in accordance with earlier studies. The GOME-2 and OMI satellite columns suggest a global pyrogenic flux decrease by 36 and 33 %, respectively, compared to the GFEDv3 inventory. This decrease is especially pronounced over tropical forests such as Amazonia and Thailand/Myanmar, and is supported by comparisons with IASI CO observations. In contrast to these flux reductions, the emissions due to harvest waste burning are strongly enhanced in the Northeastern China plain in June (by ca. 70 % in June according to OMI) as well as over Indochina in March. Sensitivity inversions showed robustness of the inferred estimates, which were found to lie within 7 % of the standard inversion results at the global scale.

1 Introduction

Besides a small direct source, the dominant source of formaldehyde (HCHO) is its photochemical formation due to the oxidation of methane and non-methane volatile organic compounds (NMVOCs) emitted by the biosphere, vegetation fires and human activities. Methane oxidation is by far the largest contributor to the HCHO formation (ca. 60 % on the global scale), while the remainder is due to oxidation of a large variety of VOCs of anthropogenic, pyrogenic and biogenic origin (Stavrakou et al., 2009a). The main removal processes (Sander et al., 2011) are the oxidation by OH,

$$HCHO + OH(+O_2) \rightarrow CO + HO_2 + H_2O,$$

ultimately producing CO and converting OH to HO_2, and photolysis reactions

$$HCHO + h\nu \rightarrow CO + H_2, \text{ and}$$
$$HCHO + h\nu(+2O_2) \rightarrow CO + 2HO_2,$$

ACPD
15, 12007–12067, 2015

producing CO as well as HO_2 radicals.

Because of its short photochemical lifetime (ca. 4–5 h), and of the short lifetime of its main NMVOC precursors, most importantly isoprene, enhanced levels of HCHO are directly associated with the presence of nearby hydrocarbon emission sources. The strong potential of HCHO measurement to constrain VOC emission fluxes on global and regional scales was put forward through a large body of literature studies, relying on the measurement of HCHO column densities from space by solar backscatter radiation in the UV-Visible spectral region (Chance et al., 2000; Palmer et al., 2003, 2006; Millet et al., 2006, 2008; Dufour et al., 2009; Barkley et al., 2009; Stavrakou et al., 2009a, b; Marais et al., 2012, 2014). In some cases, however, these studies led to conflicting answers regarding the magnitude and/or spatiotemporal variability of the underlying VOC sources, mostly owing to differences in the satellite column products, in the models used to infer top-down estimates through inversion techniques, and in the emission inventories used as input in the models. The latter point is very often a source of confusion, since a very large range of estimates can be obtained using the same emission model depending on the choice of input variables. Indeed, the isoprene fluxes estimated using MEGAN (Guenther et al., 2006), the most commonly used bottom-up emission model for biospheric emissions, are found to strongly vary depending on the driving variables used (e.g. meteorology, landcover), leading to an uncertainty of about a factor of 5 for the global isoprene emissions (Arneth et al., 2011) and underscoring the need for clearly indicated a priori emission information in order to allow meaningful comparisons between inverse modelling studies.

Despite significant progress in the field, the derivation of VOC emissions using HCHO columns remains challenging, mainly owing to the large number and diversity of HCHO precursors, to uncertainties regarding their sources and speciation profiles, and to inadequate or incomplete knowledge of their chemical mechanisms and pathways leading to HCHO formation. In addition, it crucially depends on the quality of the satellite retrievals, and therefore efforts to address aspects such as instrumental degradation, temporal stability of the retrievals, noise reduction, and error characterization

ACPD
15, 12007–12067, 2015

are of primary importance (De Smedt et al., 2012, 2015; Hewson et al., 2013; González Abad et al., 2015). The diurnal cycle of HCHO concentrations has been investigated in field studies in different environments. At a tropical forest location in Borneo, a midday peak followed by gradual decrease in the evening were observed (MacDonald et al., 2012). At a forest site in California, HCHO concentration was observed to peak in the evening during cool days and around midday under warm and sunny conditions (Choi et al., 2010). Similar diel patterns were observed near a city location in the Po valley (Junkermann, 2009). Generally, the diurnal patterns of surface HCHO concentrations are found to be mostly influenced by the magnitude of precursor emissions and their diurnal variability, as well as the development of the boundary layer. Diurnal measurements of HCHO columns are unfortunately more limited. Measurements over the remote ocean using the MAX-DOAS technique showed noontime maxima and low morning and evening values (Peters et al., 2012). The observation of HCHO columns by GOME-2 and OMI at different times (09:30 and 13:30 LT) offer a potentially useful additional piece of information in this respect.

Our first objective is to investigate the diurnal variability of HCHO columns simulated by the IMAGESv2 global CTM, and in particular, to evaluate the model capability to reproduce the observed diurnal cycle of HCHO columns at different locations. The main focus of this study is to address the issue of consistency between VOC flux strengths inferred from one complete year of GOME-2 and OMI HCHO column densities, taking into account their different instrument overpass times. For that purpose, the satellite algorithms developed for the two sensors were designed to ensure the maximum consistency between the two sets of observations (De Smedt et al., 2015). The inversion framework uses the adjoint model (Müller and Stavrakou, 2005; Stavrakou et al., 2009a) and fluxes are optimized per month, model grid and emission category (anthropogenic, biogenic and pyrogenic). The same inversion setup is applied using either GOME-2 or OMI measurements as top-down constraints for 2010, a particularly warm and dry year with intense fires and enhanced biogenic emissions. Sensitivity studies

ACPD
15, 12007–12067, 2015

are carried out to assess the robustness of the findings to different assumptions, e.g. to the inversion design.

In Sect. 2 a brief description of the IMAGESv2 model is given, with particular focus on the formation of HCHO in the oxidation of anthropogenic VOCs (Sect. 2.2). The modelled and observed diurnal cycle of HCHO columns is discussed in detail in Sect. 3. The GOME-2 and OMI HCHO columns are briefly discussed in Sect. 4. An overview of the emissions inferred from the inversions using GOME-2 and OMI data, as well as global results from sensitivity case studies are presented in Sect. 5. The VOC emissions inferred at the mid-latitudes (North America, China) and in tropical regions (Amazonia, Indonesia, Indochina, Africa) are thoroughly described in Sects. 6 and 7. Finally, conclusions are drawn in Sect. 8.

2 HCHO simulated with IMAGESv2

2.1 Brief model description

The IMAGESv2 global CTM is run at $2^{\circ} \times 2.5^{\circ}$ horizontal resolution and extends vertically from the Earth's surface to the lower stratosphere through 40 unevenly spaced sigma-pressure levels. It calculates daily averaged concentrations of 131 transported and 41 short-lived trace gases with a time step of 6 h. The effect of diurnal variations are considered through correction factors on the photolysis and kinetic rates obtained from model simulations accounting for the diurnal cycle of photorates, emissions and meteorological variables (Stavrakou et al., 2009a). A thorough model description is given in Stavrakou et al. (2013) and references therein. The target year of this study is 2010.

Anthropogenic emissions are obtained from the RETRO 2000 database (Schultz et al., 2008), except over Asia where the REASv2 inventory for year 2008 is used (Kurokawa et al., 2013). The diurnal profile of anthropogenic emissions follows Jenkin et al. (2000). Isoprene emissions (including their diurnal, day-to-day and sea-

ACPD
15, 12007–12067, 2015

sonal variations) are obtained from the MEGAN-MOHYCAN-v2 inventory (http://tropo.aeronomie.be/models/isoprene.htm, Müller et al., 2008; Stavrakou et al., 2014) and are estimated at 363 Tg in 2010 (Fig. 1). Open vegetation fire emissions are taken from GFEDv3 (van der Werf et al., 2010), with emission factors for tropical, extratropical, savanna and peat fire burning provided from the 2011 update of the recommendations by Andreae and Merlet (2001). The GFEDv3 emission is estimated at 105.4 TgVOC in 2010, equivalent to 2.26 Tmoles (average molecular weight of 46.5) (Fig. 1). The diurnal profile of biomass burning emissions was derived based on a complete year of geostationary active fires and fire radiative power observations from the SEVIRI imager over Africa (Roberts et al., 2009). The analysis of the fire cycle, performed over 20 different land cover types in the Northern and Southern Hemisphere Africa, exhibits strong diurnal variability and very similar patterns in both hemispheres. According to this dataset, fire activity is negligible during the night and low in the early morning, it peaks around 13:30 LT, and decreases rapidly in the afternoon hours. The African diurnal profile has been applied to all fires worldwide. The vertical profiles of pyrogenic emissions are taken from a new global dataset (Sofiev et al., 2013) of vertical smoke profiles from open fires, based on plume top heights computed by a semi-empirical model (Sofiev et al., 2012), and fire radiative power from the MODIS instrument. These profiles are highly variable depending on the season and the year. Forest regions are characterized by high altitude plumes (up to 6–8 km), whereas grasslands generally emit within 2–3 km. About half of emitted flux is injected within the boundary layer. The 5th, median, 80th and 99th monthly percentiles of injection profiles maps of this dataset were obtained from the GlobEmission website (http://www.globemission.eu) and implemented in the CTM.

The chemical mechanism of isoprene oxidation accounts for OH recycling according to the Leuven Isoprene mechanism LIM0 (Peeters et al., 2009; Peeters and Müller, 2010; Stavrakou et al., 2010), and its upgraded version LIM1 (Peeters et al., 2014). LIM1 is based on a theoretical re-evaluation of the kinetics of isoprene peroxy radicals undergoing 1,5 and 1,6-shift isomerization, and is found to be in satisfactory agree-

ACPD
15, 12007–12067, 2015

ment (factor of ∼ 2) with experimental yields of the hydroperoxy aldehydes (HPALDs) believed to be major isomerization products (Crounse et al., 2011). Based on box model calculations using the KineticPreProcessor (KPP) chemical solver (Damian et al., 2002), the isomerization of isoprene peroxy radicals is estimated to decrease the molar HCHO yield by ∼ 8 % in high NO_x conditions (2.39 vs. 2.60 mol mol^{-1} after two months of simulation at 1 ppbv NO_2), and by ∼ 15 % in low NO_x conditions (1.91 vs. 2.25 after two months at 0.1 ppbv NO_2). These estimated changes are however very uncertain, given their dependence on the unimolecular reaction rates of isoprene peroxy radicals and on the poorly constrained fate of the isomerization products.

2.2 HCHO from anthropogenic NMVOC emissions

Based on the NMVOC speciation profile of the UK National Atmospheric Emissions Inventory (NAEI) (Goodwin et al., 2001), 49 out of the 650 considered compounds account for ca. 81 % of the total UK emission. 17 of the 49 compounds are included explicitly in IMAGESv2, namely, ethane, propane, ethene, propene, acetylene, formaldehyde, acetaldehyde, propanal, benzene, toluene, xylenes, methanol, ethanol, formic acid, acetic acid, acetone, and methyl ethyl ketone. The remaining 32 species (Table 1) are taken into account through a lumped compound, OAHC (other anthropogenic hydrocarbons). The oxidation mechanism of OAHC is adjusted in order to reproduce the yields of HCHO from the mix of 32 higher NMVOCs. This adjustment is realized based on time-dependent box model calculations using the semi-explicit Master Chemical Mechanism (MCMv3.2, http://mcm.leeds.ac.uk/MCM/, Saunders et al., 2003; Bloss et al., 2005).

The simulations start at 6 a.m. for a temperature of 300 K at a mid-latitude location (30° N) in June. The initial concentrations of O_3, CO, and OAHC are set at 35, 200 and 1 ppb, respectively. The NO_2 concentration is kept equal to 1 ppb since our focus is on environments dominated by anthropogenic activities. For each NMVOC, the HCHO yield is calculated after one day of simulation (short-term) and after 60 days (final). The short-term yield is defined as $Y_{1d} = P_{1d}/C_0$, where C_0 is the initial OAHC concentration

ACPD
15, 12007–12067, 2015

and P_{1d} is the HCHO produced after one day. The final yield is calculated as $Y_{60d} = P_{60d}/\Delta C$, ΔC being the difference between the initial and the final OAHC concentration. Whereas the final yield is most relevant for estimating the impact of a precursor VOC on the global HCHO budget, the short-term yield best reflects the impact of this compound in the vicinity of its emission region.

The calculated short-term and final molar yields are summarized in Table 1. As expected, the highest short-term yields are calculated for the most reactive precursors, namely, the higher alkenes and aromatics, with k_{OH} typically ranging between 3×10^{-11} and 7×10^{-11} cm^3 molec^{-1} s^{-1}. For those compounds, the short-term yield and the final yield are very close, within ~ 10 %. Exceptions are the cases of ethylbenzene, which is less reactive, and 2-methylpropene, which is oxidized to acetone, a very slow-reacting intermediate. For alkanes, alcohols and esters, the short-term yield is often much lower than the final yield, due to the relatively low reactivity of the precursor (k_{OH} between 2×10^{-12} and 13×10^{-12} cm^3 molec^{-1} s^{-1}) and/or due to the existence of slow-reacting oxygenated intermediates.

For alkanes, the highest final yields are calculated for branched-chain structures (0.5–0.66 per carbon). The yields are slightly lower for butane and pentane (0.5 C^{-1}) and significantly lower for the longer linear alkanes (< 0.4 C^{-1}). Final yields range between 0.43 and 0.72 C^{-1} for alkenes, and between 0.33 and 0.35 for trimethylbenzenes.

The production of HCHO (in g) by a NMVOC can be expressed as

$$P = E \cdot Y \cdot \mathrm{MW}_{\mathrm{HCHO}}/\mathrm{MW}_{\mathrm{NMVOC}}, \quad (1)$$

with E the emission (in g), Y the calculated short-term or final molar yield and MW the molecular weight.

The emission of the lumped OAHC species being taken equal to the total emission (in g) of the explicit NMVOCs, its molecular weight is calculated using

$$\mathrm{MW}_{\mathrm{OAHC}} = \frac{\sum_i E_i}{\sum_i (E_i/\mathrm{MW}_i)}, \quad (2)$$

ACPD
15, 12007–12067, 2015

and its short-term and final yield by

$$Y_{\mathrm{OAHC}} = \frac{\sum_i (E_i/\mathrm{MW}_i)\cdot Y_i}{\sum_i E_i/\mathrm{MW}_i}. \quad (3)$$

The values obtained in this way are 73 g mol^{-1} for $\mathrm{MW}_{\mathrm{OAHC}}$ and 0.567 and 2.381 for the short-term and final yields, respectively.

The rate of the reaction of OAHC with OH,

$$\mathrm{OAHC} + \mathrm{OH} \rightarrow \mathrm{KO}_2 \quad (4)$$

needed to reproduce those yields is relatively low (1.7×10^{-12} cm^3 molec^{-1} s^{-1}) based on box model calculations. The following simple mechanism is adopted:

$$\mathrm{KO}_2 + \mathrm{NO} \rightarrow 0.1\,\mathrm{KONO}_2 + 0.9\,(\mathrm{KO} + \mathrm{NO}_2) \quad (5)$$

$$\mathrm{KO}_2 + \mathrm{HO}_2 \rightarrow \mathrm{KOOH} \quad (6)$$

$$\mathrm{KO}_2 + \mathrm{CH_3O_2} \rightarrow 0.6\,(\mathrm{KO} + \mathrm{CH_3O}) + 0.2\,(\mathrm{KOH} + \mathrm{HCHO}) + 0.2\,(\mathrm{MEK} + \mathrm{CH_3OH}), \quad (7)$$

where MEK denotes methylethyl ketone, KOH is a generic higher alcohol and the oxy radical (KO) reacts immediately following

$$\begin{aligned}\mathrm{KO} \rightarrow\ & 0.14\,\mathrm{CH_3COCH_2O_2} + 0.14\,\mathrm{HO_2} \\ & + 0.32\,\mathrm{HOCH_2CH_2O_2} + 0.46\,\mathrm{CH_3CHO} \\ & + 0.46\,\mathrm{CH_3CO_3} + 0.08\,\mathrm{CH_3COCH_3}.\end{aligned}$$

Both $\mathrm{KONO_2}$ and KOOH photolyze (to $\mathrm{KO} + \mathrm{NO_2}$ and KO + OH, respectively) and react with OH:

$$\mathrm{KONO_2} + \mathrm{OH} \rightarrow \mathrm{NO_2} + \mathrm{CH_3CHO} + \mathrm{CH_3CO_3} \quad (8)$$

$$\mathrm{KOOH} + \mathrm{OH} \rightarrow 0.4\,(\mathrm{BIACET} + \mathrm{OH} + \mathrm{CH_3COCH_2O_2}) + 0.1\,\mathrm{KO_2}, \quad (9)$$

where BIACET denotes biacetyl ($\mathrm{CH_3COCOCH_3}$). The kinetic rates are $k_5 = 2.54 \times 10^{-12}\exp(360/T)$, $k_6 = 1.82\times10^{-13}\exp(1300/T)$, $k_7 = 3.8\times10^{-13}$, $k_8 = 10^{-12}$, and $k_9 = 3.9 \times 10^{-11}$ (in cm^3 molec^{-1} s^{-1}), where T denotes the temperature.

ACPD
15, 12007–12067, 2015

3 Diurnal cycle of HCHO columns

3.1 Model processes and sensitivity

The top-down determination of VOC emissions based on GOME-2 and OMI data assumes that the model reproduces reasonably well the diurnal cycle of HCHO columns. To test this assumption would require a large number of well distributed ground-based observations, which are however scarce and intermittent. We present further below a comparison with a limited dataset of column observations at surface sites, most of which are located at or near pollution centers at mid-latitudes. In order to better characterize the diurnal cycle and to identify the factors influencing it in the model, we present on Fig. 2 the modelled diurnal variations of HCHO columns at selected locations, and on Fig. 3 the distribution of the local time of the maximum in the diurnal cycle of HCHO columns. Figure 2 also shows the results of sensitivity calculations either neglecting the diurnal cycle of emissions (in blue) or neglecting biomass burning emissions (in orange), in comparison to the standard model results (in red). Several additional sensitivity simulations were conducted, the results are however not shown here for the sake of clarity.

A striking feature of Figs. 2 and 3 is the large diversity of diurnal profiles accross the seasons and locations. Very little HCHO variations are seen at high latitudes during the winter, due to the very low photochemical activity and absence of notable emissions. In regions where anthropogenic emissions are the dominant source of HCHO precursors, such as Northwestern Europe, Eastern China, India and the Middle East (Fig. 1), the diurnal cycle displays a midday maximum and a minimum at the end of the night (Fig. 2, S. England and Fig. 3). As can be seen in Fig. 2, the diurnal cycle of anthropogenic emissions has a very small impact at these locations. This is due to the fairly long photochemical lifetimes of most anthropogenic NMVOCs. Their relatively low short-term HCHO yields in comparison with the final yields (see Table 1) implies that most HCHO formation occurs days after the precursor has been emitted. The midday

ACPD
15, 12007–12067, 2015

maximum therefore reflects the diurnal cycle of OH concentrations, very low at night and maximum when radiation is highest (Logan et al., 1981).

Over the Eastern US, the wintertime (November to March) diurnal cycle displays a similar pattern due to anthropogenic emissions. In the summer, however, when biogenic isoprene is the dominant VOC, a completely different behavior is predicted, with a noon minimum and a maximum in the evening or even in the early morning (Fig. 2, Arkansas and Fig. 3). A relatively similar pattern is found in the Manaus region in the Amazon in July–September (Fig. 2), in agreement with a previous modelling study using GEOS-Chem and focussing on Amazonia (Barkley et al., 2011). At all sites impacted by isoprene (Arkansas, Borneo, Manaus and Mato Grosso), the simulation neglecting diurnal variations of emissions (Fig. 2, blue curve) leads to a continuous HCHO buildup during the night and to a pronounced morning maximum followed by a gradual decrease during daytime until a minimum in late afternoon or early evening. The nighttime buildup in that simulation follows the slow isoprene oxidation (mostly by ozone) and the near-absence of HCHO sinks, whereas the gradual HCHO decrease during the day reflects the decline of the accumulated isoprene and intermediate oxidation products due to OH oxidation. Although the daytime chemical lifetime of isoprene is short (less than 1 h at an OH concentration of 4×10^6 molec cm^{-3}), a large fraction of the formaldehyde production due to isoprene involves longer-lived intermediates (such as methylvinylketone, methacrolein, hydroxyacetone, hydroperoxides, etc.) resulting in a delayed formaldehyde production.

When the diurnal cycle of isoprene emissions is taken into account (Fig. 2, red curve), the midday emission maximum leads to a HCHO minimum and to an increase afterwards, due to the delayed production from isoprene (Arkansas, Manaus and Mato Grosso). It has been pointed out (Barkley et al., 2011) that the nighttime HCHO accumulation and morning maximum near Manaus in September might be unrealistic, as models are often unable to reproduce the observed rapid decline of isoprene concentrations during the evening at different surface sites. Nighttime chemistry, deposition and boundary layer processes might indeed be poorly represented in models, causing

ACPD
15, 12007–12067, 2015

significant deviations from the patterns described above. As is obvious from Figs. 2 and 3, different locations or seasons display often very different diurnal patterns, for complex reasons including radiation and NO_x levels, the occurrence of biomass burning, mixing processes, etc. Note however, that sensitivity simulations neglecting the diurnal cycle of boundary layer mixing and deep convection fluxes were found to cause only minimal deviations from the columns of the standard model calculations.

Vegetation fires are found to cause locally very strong variations with maximum values in the evening, exceeding by up to 70 % the morning minimum value (Central Alaska in May and July, Mato Grosso in September). As seen on Fig. 3, strong emissions over Eastern Siberia, European Russia, Central Canada, Angola, Brazil and Northern Australia are most often associated with HCHO column maxima in the late afternoon and evening.

3.2 Model evaluation

To evaluate the model diurnal cycle, we use ground-based remote-sensed measurements at the 7 following sites:

1. Cabauw/the Netherlands (52° N, 5° E), 8 June–21 July 2009 (Pinardi et al., 2013).
2. Observatoire de Haute Provence (OHP)/France (43.94° N, 5.71° E), 26 June 2007–20 March 2013 (Valks et al., 2011).
3. Uccle/Belgium (50.78° N, 4.35° E), 1 May 2011–23 April 2012 (Gielen et al., 2014).
4. Beijing/China (39.98° N, 116.38° E), 3 July 2008–17 April 2009 (Vlemmix et al., 2015, see also Hendrick et al., 2014).
5. Xianghe/China (39.75° N, 116.96° E), 7 March 2010–26 December 2013 (Vlemmix et al., 2015, see also Hendrick et al., 2014).
6. Bujumbura/Burundi (3° S, 29° E), 25 November 2013–22 January 2014 (De Smedt et al., 2015).

ACPD
15, 12007–12067, 2015

7. Reunion Island/France (20.9° S, 55.5° E), 1 August–25 October 2004, 21 May–15 October 2007, 2 June–28 December 2009, and 11 January–16 December 2010 (Vigouroux et al., 2009).

The MAX-DOAS (Multi-axis differential optical absorption spectroscopy) technique (Hönninger et al., 2004; Platt and Stutz, 2008) was used in all cases, except at Reunion Island where the FTIR (Fourier Transform infrared spectroscopy) technique is used (Griffiths and de Haseth, 2007; Vigouroux et al., 2009). Total HCHO columns are measured at all stations, and profiles are also measured at Beijing, Xianghe, and Bujumbura. Figures 4 and 5 illustrate the diurnal cycle of observed and modelled HCHO columns seasonally averaged and normalized by their noon values. The ratio of the observed columns at 13:30 and 09:30 LT ranges mostly between 0.8 and 1.2, although values close to 1.4 are found at one site (OHP). The modelled values of this ratio are most often higher than in the measurements, except at OHP. The average ratio at all sites and seasons is slightly higher in the model (1.126) than in the data (1.043), although the average absolute deviation between model and data is large (20 %), presumably mostly because of representativity issues. The coarse resolution of the model makes it impossible to reproduce the very large differences seen, for example, between the observed diurnal profiles at Beijing and Xianghe, two very nearby sites lying in the same model grid cell. OHP similarly lies in a region with strong gradients in the diurnal behavior of the columns, as seen in Fig. 3.

Nevertheless, the diurnal cycle of HCHO columns at the four most polluted sites (Uccle, Cabauw, Beijing and Xianghe) shows a consistent pattern during summertime (also in spring and fall at Uccle) which is well reproduced by the model. At Reunion Island as well, the observed midday maximum is well reproduced by the model. As pointed out above, the midday maximum at both very remote and very polluted sites is primarily caused by the diurnal cycle of OH levels, as the reaction with OH of the (mostly fairly long-lived) anthropogenic VOCs as well as methane is the main source of HCHO in those areas. In the Beijing area, the diurnal cycle of emissions is respon-

ACPD
15, 12007–12067, 2015

sible for a slight delay in the maximum towards the afternoon, in agreement with the observations.

A broader network of measurements would be necessary to provide a more detailed assessment of HCHO column diurnal variations, in particular over forests and in biomass burning areas. Nevertheless, the comparison presented above with the limited dataset of available measurements revealed no large systematic discrepancies, except for a slight overestimation (by 8 %) of the average ratio of 13:30 to 09:30 LT columns.

4 Satellite observations

The current version (v14) of the HCHO retrievals applied to GOME-2/METOP-A and OMI/AURA measurements is based on the algorithm developed for GOME-2 (version 12, De Smedt et al., 2012), but with significant adaptations, as detailed below.

A classical DOAS algorithm is used, including three main steps: (1) the fit of absorption cross-section databases to the measured Earth reflectance in order to retrieve HCHO slant columns, (2) a background normalization procedure to eliminate remaining unphysical dependencies, and (3) the calculation of tropospheric air mass factors using radiative transfer calculations and modelled a priori profiles. In GOME-2 v12, two fitting intervals were introduced to improve the treatment of BrO absorption features, and to reduce the noise on the HCHO columns (328.5–359 nm for the pre-fit of BrO, 328.5–346 nm for the fit of HCHO) (De Smedt et al., 2012).

In the current version, a third fitting interval (339–364 nm) is used to pre-fit the O_2-O_2 slant columns in order to minimize the effect of spectral interferences between the molecular absorptions. This results in a global reduction of the HCHO slant columns over the continents compared to the previous version, by 0 to 25 %, depending on the season and the altitude. It is interesting to note that the effect is very similar when applied to GOME-2 and OMI HCHO retrievals, i.e. it has little or no impact on the diurnal variations (De Smedt et al., 2015). In order to improve the fit of the slant columns, an iterative DOAS algorithm for removal of spike residuals has been implemented (Richter

ACPD
15, 12007–12067, 2015

et al., 2011). In addition, this version of the algorithm makes use of radiance spectra, daily averaged in the equatorial Pacific, which serve as reference spectra. The background normalisation now depends on the day, the latitude, but also on the viewing zenith angle of the observation. This also serves as destriping procedure, needed for an imager instrument such as OMI (Boersma et al., 2011). The air mass factor calculation is based on Palmer et al. (2001). Scattering weighting functions are calculated with the LIDORT v3.3 radiative transfer model (Spurr, 2008).

The a priori profile shapes are provided by the IMAGES model, at 09:30 LT for GOME-2 and 13:30 LT for OMI (cf. Sect. 2). The OMI-based surface reflection database from Kleipool et al. (2008) is used for both GOME-2 and OMI. Radiative cloud effects are corrected using the independent pixel approximation (Martin et al., 2002) and the respective cloud products of the instruments provided by the TEMIS website (http://www.temis.nl), namely the GOME-2 O_2 A-band Frescov6 product (Wang et al., 2008) and the OMI O_2-O_2 cloud product (Stammes et al., 2008). As for the previous algorithm versions, v14 HCHO columns are openly available on the TEMIS website (http://h2co.aeronomie.be/).

Monthly averaged HCHO columns from both instruments gridded onto the resolution of the model are used as top-down constraints. Columns with a cloud fraction higher than 40 % are excluded from the averages. HCHO data are also excluded over oceanic IMAGES gridcells (for which the land fraction is lower than 0.2), since we aim to constrain only continental sources, as well as in the region of the South Atlantic geomagnetic anomaly, i. e. within less than 1500 km of its assumed epicentre (47.0° W, 24.9° S). Finally, regridded columns for which the monthly and spatially averaged retrieval error exceeds 100 % are also rejected. The error of the satellite columns is defined as the square root of the squared sum of the retrieval error and an absolute error of 2×10^{15} molec cm^{-2}. In most VOC-emitting regions the error ranges between 40 and 60 %.

The monthly regridded HCHO columns from GOME-2 and OMI are shown in Fig. 6 for July 2010. As seen on this figure, and discussed in De Smedt et al. (2015), the early

ACPD
15, 12007–12067, 2015

afternoon columns of OMI are higher than the mid-morning values of GOME-2 at mid-latitudes, while the reverse is true at most tropical locations, in qualitative agreement with the ground-based measurements and modelling results (Figs. 4 and 5).

5 Overview of the results

Table 2 summarizes the source inversions carried out in this study. In each inversion, the emission rates of the three emission categories (anthropogenic, biogenic and biomass burning) are adjusted per month and per model grid so as to minimize a cost function measuring the overall bias between the model and a set of observations, i.e. GOME-2 or OMI HCHO columns. On the global scale, ca. 63 000 flux parameters are varied. The emission of a grid cell is not optimized when its maximum a priori monthly value is lower than 10^{10} molec cm^{-2} s^{-1}. The assumed error on the a priori anthropogenic emission by country is set equal to a factor 1.5 and 2 for OECD and other countries, respectively, to a factor of 2 for biogenic emissions and 3 for fire burning emissions. More details about the inversion framework can be found in Stavrakou et al. (2009b).

The sensitivity studies (Table 2) aim at assessing the impact of (i) the choice of a priori errors on the emission fluxes (OMI-DE, OMI-HE), (ii) the cloud fraction filter applied to the satellite data (OMI-CF), and (iii) the isomerization of isoprene peroxy radicals (OMI-IS). The annual a priori and top-down fluxes of the two standard and the four sensitivity inversions are summarized in Table 3. The a priori model columns calculated at 09:30 and 13:30 LT local time are generally higher than the GOME-2 or OMI HCHO column abundances (Fig. 6), e. g. over Europe, Southern China, the United States, Amazonia and Northern Africa. They are however found to agree generally well in terms of seasonality (Fig. 7).

Globally, the cost function is reduced by a factor of 2 after optimization, and its gradient is reduced by a factor of ca. 10^3. In general, the consistency between the two inversions is found to be highest in tropical regions. At mid-latitudes, the emission up-

ACPD
15, 12007–12067, 2015

dates (i.e. the ratios of optimized to prior emissions) are almost systematically higher in the OMI-based than in the GOME-2-based inversion. This reflects ratios of 13:30 to 09:30 LT columns which are lower in the model than suggested by the two satellite datasets.

Both GOME-2 and OMI inversions suggest a strong decrease in global biomass burning VOC emissions with regard to the a priori GFEDv3 inventory, by 36 and 33 %, respectively. This decrease is most pronounced in tropical regions. In contrast, both the OMI and GOME-2 optimizations lead to enhanced emissions (by about 50 %) due to the extensive fires which plagued European Russia in August 2010 (Sect. 6.2) and to agricultural waste burning in the North China Plain in June (Sect. 6.3). The fire burning estimates from the two base inversions are generally quite consistent, not only globally but also over large emitting regions like Amazonia, Southeastern Asia, and Africa. The sensitivity studies provide global flux estimates which are close (within 7 %) to the standard top-down results using OMI.

The globally derived isoprene fluxes are reduced in both standard inversions, by 9 % according to GOME-2 and by 13 % according to OMI, compared to the a priori estimate of the MEGAN-ECMWF-v2 inventory (363.1 Tg yr^{-1}, Table 3). The overall consistency between the global estimates is high for this emission category, despite some significant differences at a regional scale (cf. next sections). The biogenic top-down fluxes derived from the sensitivity inversions of Table 2 lie within 5 % of the OMI-based estimates on the global scale, yet larger differences are found in the regional scale.

Finally, the global anthropogenic source is decreased in the GOME-2 inversion, while it is slightly increased in the inversion using OMI. Despite their limited capability to constrain this emission category on the global scale due to its small contribution to the global HCHO budget (Stavrakou et al., 2009a), the satellite observations are found to provide constraints over highly polluted regions, notably Eastern China, where however the discrepancy between the two sensors is most evident (see Sect. 6.3).

Annual emission updates for the different source categories, and the monthly variation of the a priori and optimized flux estimates are illustrated in Figs. 9–13.

ACPD
15, 12007–12067, 2015

Modifying the errors on the flux parameters infers isoprene emission decreases of ca. 15 % (OMI-HE) and 30 % (OMI-DE) with regard to the initial isoprene inventory, and within 7 % of the standard OMI inversion, cf. Table 3. As expected, due to the limited or stronger confidence assigned to the a priori inventories in OMI-DE and OMI-HE scenarios, respectively, most substantial departures from the a priori inventory are obtained when doubling the errors on the emission parameters, while the OMI-HE scenario lies closer to the a priori database. The impact of the use of a stricter cloud criterion on the OMI scenes used as top-down constraints (20 % for OMI-CF instead of 40 % in OMI base inversion) results in weak increases of the globally inferred fluxes with respect to the OMI inversion, but the enhancement is found to be more important in extratropical regions, and amounts to 22 % for biomass burning emissions (Table 3, Fig. 8). Finally, suppressing the isomerization channel in isoprene oxidation increases the HCHO yield from isoprene and leads to slightly higher model columns over isoprene-rich regions. The resulting isoprene fluxes are found to be by 4 % lower on the global scale, but over Amazonia, the emission reduction is estimated at 8 % compared to the results of OMI inversion.

6 Emissions at the mid-latitudes

6.1 North America

Biogenic isoprene emissions drive the HCHO column seasonality and explain the summertime column peak in the Eastern US (Fig. 7). The a priori model exhibits, however, a much stronger seasonal variability than the observation with a summer-to-winter ratio of 4–5 compared to the observed ratio of about 2. In summertime, the a priori model overestimates the GOME-2 and OMI measurements by up to 50 and 35 %, respectively in the Eastern US (Figs. 6 and 7). This drives the significant decrease in the optimized isoprene fluxes, from the a priori value of 17.8 to 11.6 Tg (GOME-2) and to 13.8 Tg (OMI) over the US in 2010, in good agreement with our earlier flux estimates

ACPD
15, 12007–12067, 2015

(13 Tg yr^{-1}) based on SCIAMACHY HCHO columns (Stavrakou et al., 2009b). Even larger reductions are found in the Southeastern US, amounting to ca. 25 and 40 % in the OMI and GOME-2 inversions, respectively (Fig. 13). Anthropogenic and pyrogenic emissions over the US are essentially unchanged by the inversions. The estimated cumulative June–August US isoprene emissions from both optimizations (7.8 Tg for GOME-2 and 9.5 Tg for OMI) agree well with reported values based on earlier versions of OMI HCHO retrievals (9.3 Tg according to the variable slope technique as described in Millet et al., 2008). The OMI-based isoprene flux in July 2010, estimated at 3.23 Tg, is by 30 % lower than the a priori (4.62 Tg), corroborating the low values of the BEIS2 inventory (Palmer et al., 2003).

The model predictions are compared to HCHO measurements from the INTEX-A aircraft campaign conducted in July–August 2004 over the Eastern US (Singh et al., 2006; Fried et al., 2008) in Fig. 14. It is worth noting that the measurements by NCAR (National Center for Atmospheric Research) and URI (Univ. Rhode Island) exhibit large differences between them, the NCAR values being by ca. 50 % higher than URI below 2 km altitude (Fig. 14). The model simulations are performed for 2004, and the concentrations are sampled at the locations and times of the airborne measurements. In the a posteriori simulation shown in Fig. 14, the bottom-up isoprene emissions for 2004 were multiplied by the isoprene emission update inferred from either the OMI or the GOME-2 inversion for 2010. As seen on Fig. 14, the average HCHO concentration below 2 km altitude is decreased by about 10 % in the OMI inversion (15 % in the case of GOME-2) and remains within the range of the NCAR and URI measurements. Despite the marked underestimation of the modelled HCHO (1.39 and 1.32 ppbv in the OMI and GOME-2 inversions) in comparison to NCAR observations (1.83 ppbv), the emission optimization results in an increased Pearson's spatial correlation coeffient between the modelled and observed concentrations below 2 km, from 0.74 in the a priori to 0.79 and 0.80 in the OMI and GOME-2 inversions. A similar improvement is found with respect to URI data.

ACPD
15, 12007–12067, 2015

6.2 Russia

The a priori model underpredicts the observed OMI HCHO columns during the Russian fires of July–August 2010 by up to a factor of 2, in particular over a broad region extending to the North (61° N) and East (55° E) of Moscow (Fig. 6). Similar spatial patterns are also observed in GOME-2 HCHO columns. However, the GOME-2 columns are lower than OMI over this region, and the model underestimation is less severe in this case reaching 60 %. The lower GOME-2 values might be due to the lower retrieval sensitivity of GOME-2 to lower tropospheric HCHO compared to OMI at these latitudes, associated to larger solar zenith angles (De Smedt et al., 2015). As a result, the increase of the pyrogenic emission fluxes is strongest in the OMI inversion, from 440 Gg VOC in the GFEDv3 inventory, to 720 Gg VOC (630 GgVOC in GOME-2) in August 2010 over Europe. Accordingly, the isoprene fluxes inferred from the OMI inversion in August are also larger, about 40 % higher than the a priori estimate in the Moscow area, whereas the increase derived by GOME-2 does not exceed 25 %. Overall, the OMI data suggest annual isoprene fluxes in Europe by 11 % higher than the a priori inventory (Table 3).

Strongly enhanced fire emissions in the Moscow region between mid-July and mid-August 2010 were reported based on satellite observations of CO from MOPITT (Konovalov et al., 2011) and IASI (Krol et al., 2013; R'honi et al., 2013), and on suface measureuments (Konovalov et al., 2011). The optimized fire emission inferred by assimilation of IASI CO columns in Krol et al. (2013) lies within 22 and 27 Tg CO during the fires, i.e. about 7–10 times higher than in the bottom-up inventory (GFEDv3). These values are comparable with the ranges of 19–33 and 34–40 Tg CO suggested by R'honi et al. (2013) and Yurganov et al. (2011), respectively, but are much higher than reported values of ca. 10 Tg CO derived using surface CO measurements in the Moscow area (Konovalov et al., 2011). The latter study identifies the contribution of peat burning to the total CO fire emission in this region to be as high as 30 %.

The IMAGESv2 a priori CO simulation (using GFEDv3 inventory) underestimates substantially the IASI CO observations. Scaling the CO emissions in IMAGESv2 to the

ACPD
15, 12007–12067, 2015

fire VOC increase suggested by the OMI HCHO optimization, i.e. ca. 60 % in July and August 2010, barely improves the model agreement with the satellite, indicating that, in accordance with earlier studies, more drastic fire flux enhancements (factor of 5 to 10) are required to reconcile CO model-data mismatches. The reasons for the differences in the emission increases inferred by CO and HCHO during the 2010 Russian fires are currently unknown, but could be related either to inadequate knowledge of emission factors of CO and VOCs from peat fires, and/or underestimated remote-sensed HCHO columns over fire scenes due to possibly important aerosol effects not accounted for in the retrievals.

6.3 China

The dominant emission source in China is anthropogenic and is estimated at 25.5 Tg VOC in REASv2 (Kurokawa et al., 2013) for 2008. The biogenic source, mainly located in Southern China, amounts to 7 Tg in 2010 in the MEGAN-MOHYCAN-v2 inventory (Stavrakou et al., 2014; Guenther et al., 2006, 2012). In Northern China, the HCHO columns are underestimated by the a priori model in winter compared to OMI, whereas a relatively good agreement is found in summer. In Southern China, a general model overestimation is found all year round (Figs. 6 and 7).

Although the OMI-based inversion yields total Chinese anthropogenic emissions very similar to the a priori (24.6 Tg VOC), the emission patterns are modified with increased emissions in Northeast China and especially around Beijing (20–40 %), and emission reductions in the Southeast and in particular around Shanghai (15–47 %) and Guangzhou (15–30 %). The total GOME-2 emission, estimated at 20.6 Tg VOC, is lower than the OMI result, but in good agreement with the estimate (20.2 Tg in 2008) of the Multi-resolution Emission Inventory for China (MEIC, http://www.meicmodel.org). The flux distributions from both inversions have common features, e.g. decreased fluxes in Shanghai and Guangzhou regions, but contradicting estimates in the Northeast where GOME-2 observations do not support the emission enhancements suggested by OMI.

ACPD
15, 12007–12067, 2015

This discrepancy is primarily due to the lower modelled ratios of 13:30 to 09:30 LT columns compared to the satellite datasets (Fig. 7). Note that, however, the model was found to overestimate this ratio against MAX-DOAS data at Beijing and Xianghe (Fig. 5). Another possible cause for difference between the OMI and GOME-2 results is the limited availability of GOME-2 data in wintertime (Fig. 7) due to the high solar zenith angles leading to large retrieval errors frequently exceeding 100 %. For example, GOME-2 columns are unavailable from November to April over Beijing.

In the North China Plain, one of the largest agricultural plains on Earth, the post wheat harvest season fires set up every year in June is a common farmer's practice (Huang et al., 2012), responsible for poor air quality conditions and environmental harm (Yamaji et al., 2010). Both OMI and GOME-2-based inversions suggest a considerable enhancement of the agricultural fire flux in this region, by almost a factor of 2 in comparison with the a priori inventory by Huang et al. (2012), cf. Fig. 12. The interannual variability of these emissions will be addressed in a separate work in preparation.

Finally, the Chinese isoprene emission are decreased from 7 Tg year^{-1} to 6.5 Tg (OMI) and 5.9 Tg (GOME-2), with especially strong decreases in Southern China, as illustrated in Fig. 10.

7 Emissions in the Tropics

7.1 South America

After the 2005 drought in Amazonia, characterized as one-in-a-century event (Marengo et al., 2008), Amazonia suffered a second, even more severe drought in 2010 with major environmental impacts (Marengo et al., 2011). Extensive wildfires broke out in different regions from July to October, with central and south Amazonia as main epicenters. The massive fire burning is reflected in the high HCHO columns (up to 15×10^{15} molec cm^{-2}) detected by GOME-2 and OMI during these months, about twice the observed columns in the wet season (Fig. 7). Both instruments agree very well on

ACPD
15, 12007–12067, 2015

the magnitudes and spatial patterns of the HCHO columns, as illustrated in Fig. 15. The a priori model strongly overestimates the observations during the dry season (by up to 70 % in August) indicating that the GFEDv3 emissions for this region are most likely too high. The GOME-2 and OMI inversions decrease the fire emission by factors of 2 and 2.5, respectively (Fig. 12). Even stronger decreases (factor of 3) are found over Northern Bolivia and central Amazonia (Fig. 9).

These emission reductions are supported by comparison with CO columns observed by the Infrared Atmospheric Sounding Interferometer (IASI) instrument on the MetOp payload (George et al., 2009). The use of fire emissions from GFEDv3 leads to strongly overestimated CO columns in comparison to IASI observations in August 2010 (Fig. 15), reaching almost a factor of 2 over Western Amazonia. Significant improvement in the model-data match is achieved when the emission reduction inferred by the OMI-based inversion is implemented and applied not only to NMVOCs but also to other compounds including CO. The GFEDv3 emissions of CO in 2010 were also found to be substantially overestimated, by a factor of ~ 1.8 over South America between 5 and 25° S, by inverse modelling of MOPITT CO columns using the GEOS-Chem model (Bloom et al., 2015). The most likely cause for the lower emissions in 2010 compared to 2007 was proposed by these authors to be a reduction of the combusted biomass density possibly due to dry conditions and/or repeat fires. The good consistency found between results using either CO or HCHO indicates that the emission factors used in the model for NMVOC and CO (or at least their ratios) are appropriate, unless an error compensation is responsible for the noted good agreement. Note also that, besides the good consistency found between the emission estimates derived from GOME-2 and OMI, the performed sensitivity inversions induce only very weak departures from the standard inversion (Fig. 12).

Isoprene fluxes over Amazonia derived by GOME-2 and OMI inversions are estimated at 73.7 and 92.5 Tg, respectively. This is by 25 and 7 % lower than the prior and in good agreement with previous studies using satellite HCHO observations from the SCIAMACHY instrument (Stavrakou et al., 2009b). The seasonal variation of the pos-

ACPD
15, 12007–12067, 2015

terior fluxes is found to be consistent with the a priori inventory, except during the transitional wet-to-dry period (April–June) with both GOME-2 and OMI satellite datasets pointing to a significant flux decrease by ca. 25 % (Fig. 13). This behaviour confirms previous comparisons using GOME HCHO observations suggesting that factors other than the temperature influence the observed variability (Barkley et al., 2008), such as the growth of new leaves causing a temporary shut-down of the emissions (Barkley et al., 2009).

7.2 Indonesia

Fire activity was exceptionally low in 2010, with annual emissions of about 0.1 Tg VOC, i.e. about two orders magnitude less than for high years such as 2006 according to GFEDv3.

The GOME-2 and OMI inferred isoprene estimates show good consistency over Indonesia all year round, amounting to 10.3 and 11.1 Tg, respectively, close to the a priori (11.6 Tg). The inferred isoprene emissions are, however, twice lower than reported fluxes of 25 $\mathrm{Tg\,yr^{-1}}$ based on SCIAMACHY HCHO observations, which were themselves decreased with respect to their priori isoprene flux of 35 $\mathrm{Tg\,yr^{-1}}$ (Stavrakou et al., 2009b). In comparison to that study, the isoprene a priori emissions used in the present work are strongly reduced over this region, due to a drastic reduction by a factor of 4.1 of the MEGANv2.1 basal isoprene rate for tropical rainforests over Asia, as suggested by field measurements in Borneo (Langford et al., 2010). This reduction implemented in the MEGAN-MOHYCAN-v2 model (Stavrakou et al., 2014) is found here to be corroborated by GOME-2 and OMI HCHO measurements.

7.3 Indochina

The Northern part of the Indochinese peninsula (primarily Myanmar, also Assam in India and parts of Thailand) faces intense forest fires during the dry season, as very well seen in the GOME-2 and OMI HCHO timeseries, with values reach-

ACPD
15, 12007–12067, 2015

ing 15×10^{15} molec cm^{-2} in March, about three times higher than in the wet season (Fig. 7).

Both the GOME-2 and OMI data point to substantial, but very contrasted updates in the pyrogenic fluxes during the fire season (March, Fig. 9): flux reductions by a factor of 2–5 over Myanmar and surrounding forested areas, and flux increases by a factor of almost 2 (or more in the case of OMI) over the Southeastern part of the peninsula, which includes Cambodia, Southern Laos and Southern Vietnam. In the OMI-DE inversion assuming doubled errors on the a priori fluxes, the updates are even more pronounced and reach a factor of 4 over parts of Vietnam and Laos. The annual emissions in the entire region are decreased by 15 and 26 % in the OMI and GOME-2 inversions, respectively. As illustrated in Fig. 16, the optimization leads to a substantial improvement of the model performance, although the HCHO columns remain significantly underestimated (by up to 20 %) in the Southern part of the peninsula (e. g. Cambodia), most likely due to a too strong underestimation of the GFEDv3 emissions used as a priori in the model. The emission drop over Myanmar and the need for higher emissions in the Southeast are partly confirmed by comparisons with IASI CO columns. Indeed, modelled CO simulations using either GFEDv3 or biomass burning fluxes optimized using OMI data (Fig. 16) display a better agreement in the second case, despite an underestimation of CO by ca. 10 % over most of the peninsula.

The strong enhancement of pyrogenic emissions required to comply to the satellite data over the Southeastern part of Indochina might be due to the occurrence of agricultural fires in those regions (e. g. Cambodia), known to be a common management practice (Chang and Song, 2010). These fires are very difficult to detect by satellite due to their limited spatial extent. It is worth noting that the latest version of the Fire Inventory from NCAR (Wiedinmyer et al., 2011) (FINNv1.5) predicts much higher emissions from this region: ca. 43 Tg C in March in the region 100–108° E, 10–18° N, i.e. a factor of 10 higher than in the GFEDv3 inventory (4.3 Tg C). The differences between GFEDv3 and FINN are most likely due to inherent differences in the proxy variables used in the respective emission models, burned area in the case of GFEDv3, and active fire counts

ACPD
15, 12007–12067, 2015

in FINN model, both retrieved from MODIS satellite data. The two inventories provide however very similar estimates for the more forested, Northwestern part of Indochina (19–27° N, 97–100° E): 105 Tg C in GFEDv3, 124 Tg C in FINNv1.5.

Considerable cloudiness during the rainy season (May–October) causes gaps in the OMI HCHO timeseries, due to the exclusion of scenes with ≥ 40 % cloud cover. The GOME-2 data series are comparatively less affected by this issue, due to the diurnal precipitation and cloudiness patterns during the monsoon season. Indeed, long-term observations over Indochina (Takahashi et al., 2010) reveal an early afternoon rainfall peak (13:00–16:00 LT), and heavy rainfall in the early morning (04:00–07:00 LT), but lower precipitation rates between 07:00 and 10:00 LT. GOME-2 observations are therefore less contaminated by clouds and offer a better spatial coverage during the rainy season in this region.

7.4 Africa

Over Africa, the annual pyrogenic source, amounting at 40.7 Tg VOC in the a priori, is reduced to 26.2 and 32.6 Tg VOC in the GOME-2 and OMI inversions, respectively (Table 3). A smaller reduction is also inferred for isoprene fluxes, estimated at 76.6 Tg (GOME-2) and at 74.2 Tg (OMI), within 10 % of the a priori value (81.6 Tg). These estimates are in line with recently reported isoprene fluxes over Africa based on the NASA dataset of OMI HCHO columns (77 Tg C or 87 Tg isoprene compared to 116 Tg isoprene in the a priori, Marais et al., 2012). The spatial distribution of the emission updates is displayed in Figs. 9–11.

African fire occurrence peaks in central Africa (e. g., the Democratic Republic of the Congo or DRC) in early June (Fig. 7) and lasts until August with the end of the dry season. The GOME-2 and OMI observations show an excellent accordance, with morning columns being about 10 % higher than in the afternoon, consistent with measurements in Bujumbura (Fig. 5), although the morning-to-afternoon ratio was found to be higher in the ground-based observations (1.25). The model simulations overpredict the observations of both sounders during the fire season by 10–25 %. The posterior bias reduction

ACPD
15, 12007–12067, 2015

(cf. Fig. 7, DRC region) is achieved by a significant biomass burning flux decrease, reaching a factor of 2 in the southern part of DRC, and 20–30 % elsewhere between 2 and 12° S. In a similar manner, up to a factor of 2 emission decrease is also needed in the region of the Central African Republic during the fire season (November–February) to match the observed columns (Fig. 7), in good agreement with our previous study using SCIAMACHY HCHO columns (Stavrakou et al., 2009b). Only small changes are inferred for isoprene emissions in Northern Africa, by 11 % (GOME-2) and by 16 % (OMI) decrease compared to the a priori, as illustrated in Fig. 13.

In Southern Africa, biogenic fluxes are highest in January and lowest in July, while the fire season starts in May, and peaks in September (Figs. 12 and 13). Both GOME-2 and OMI inversions infer only small isoprene flux updates (Table 3). Regarding fire emissions, in constrast with GOME-2 data suggesting a ca. 30 % flux reduction (to 17.6 from 25.8 Tg VOC), the OMI-based estimate lies within 10 % of the a priori, due to a compensation of flux decreases North of approx. 15° S, and flux increases in the southernmost part of the continent, south of ca. 15° S (Fig. 9). Although the seasonal patterns are essentialy preserved by the optimization, both inversions predict higher emissions at the end of the dry season, especially over Zambia and surrounding regions (October, Fig. 12). These updates are highest (factor of ∼ 2) in the OMI optimization, but the patterns are very similar in both inversions.

8 Conclusions

The emissions of NMVOCs in 2010 were optimized by inverse modelling using the IMAGESv2 CTM and its adjoint with HCHO column abundances from either GOME-2 or OMI as observational constraint. Given their different overpass times, the consistency of the inferred emissions depends on how the model can faithfully reproduce the diurnal cycle of HCHO columns. The modelled diurnal cycle displays a great variability mirroring the competing influences of photochemical productions and losses as well as the diurnal profiles of emissions and (to a lesser extent) meteorological parameters.

ACPD
15, 12007–12067, 2015

Where anthropogenic VOCs are dominant, daytime photochemical production and the anthropogenic emission profile leads to an early afternoon maximum, in agreement with MAX-DOAS observations in Belgium, Holland and (during summertime) the Beijing area. Over oceanic areas, where methane oxidation is the only significant source in the model, a similar behavior is also simulated, in agreement with FTIR data at Reunion Island. The poor model performance at several locations (Bujumbura, OHP, Beijing in winter/spring) is likely at least partly due to the coarse model resolution, as shown by the very different diurnal profiles observed at Beijing and Xianghe. This limited representativity of local ground-based sites possibly explains (part of) the large deviations (typically ±10–30 %) found between the calculated and observed ratios of the HCHO columns at 13:30 and 09:30 LT. Despite this large scatter, the average ratio of 13:30 LT columns to 09:30 LT columns is only slightly higher (1.126) in the model compared to the MAX-DOAS and FTIR measurements (1.043).

Unfortunately no ground-based measurements are available in regions where the simulated diurnal cycle amplitude is largest, namely over intense fire scenes at both tropical and boreal latitudes. Over these regions, an evening maximum is predicted, and the peak-to-trough ratio reaches up to 70 %. In isoprene-rich areas, the diurnal HCHO cycle often, but not always, displays a minimum around noon, when the photochemical sink is highest, and a maximum in the late evening or early morning, in agreement with a previous modelling study (Barkley et al., 2011). Validation studies over forested areas will be needed to determine how realistic these patterns are.

The ratio of 13:30 to 09:30 LT column is found to be most often between 0.8 and 1.2 according to ground-based measurements. Similar, but generally higher values of this ratio are calculated by the model, by 8 % on average. The satellite, on the other hand, although in qualitative agreement with the above, suggests higher ratios of 13:30 to 09:30 LT columns than the model at mid-latitudes, whereas no clear pattern emerges in tropical regions (Fig. 7). Nevertheless, these discrepancies in terms of morning/afternoon ratios are most often small in comparison with the model/data differences in the HCHO columns themselves. As a consequence, the emission fluxes

ACPD
15, 12007–12067, 2015

inferred from both GOME-2 and OMI inversions are found to be generally very consistent. They both suggest a strong decrease of the global biomass burning source, by about 35 %. The decrease is mostly concentrated in the Tropics, e.g. over Amazonia (factor of > 2 reduction), over Equatorial Africa and over Myanmar and surrounding regions (factor of 2–5 reduction in March). These updates are confirmed by comparing CO columns predicted by the model using the biomass burning emissions estimated by the OMI inversion with IASI CO columns. The results are also consistent with a recent study using MOPITT CO columns (Bloom et al., 2015). The seasonal profile of the emissions is generally well preserved by the inversions, except for a significant enhancement near the end of the dry season, in particular over Southern Africa (in October) but also Amazonia (in September) and Indochina (in April). Both satellite datasets point to strong enhancements of agricultural fire fluxes in the North China Plain in June (factor of almost 2) and in the southern part of Indochina, compared to the a priori estimate.

Very good agreement between the inversion results is found for isoprene fluxes, with global annual fluxes reduced by 9 % (GOME-2) and 13 % (OMI) compared to the a priori of 363 Tg. In the Southeastern US, both inversions agree on a substantial decrease by ca. 25 % (OMI) and 40 % (GOME-2), in good agreement with previous estimates based on SCIAMACHY and OMI HCHO data. This reduction improves the correlation between calculated and observed HCHO concentrations during the airborne INTEX-A campaign conducted over the Eastern US. Over Amazonia, the source of isoprene is found to be consistently lower than the a priori, in particular during the wet-to-dry season transition (April–June), in accordance with previously reported estimates. Over Indonesia, the optimizations do not present significant deviations from the prior, thereby validating the a priori isoprene inventory which incorporated decreased basal emission rates for Asian tropical rainforests.

The results show that the global anthropogenic VOC fluxes are not well constrained, as indicated by the negligible updates derived by the inversions over most areas, except over highly polluted regions with a distinct anthropogenic signal in the HCHO columns,

ACPD
15, 12007–12067, 2015

like China. In this region, the changes in the emission patterns found by the OMI-based optimization are not well reproduced by the inversion of GOME-2 data, likely reflecting discrepancies in the 13:30 LT/09:30 LT column ratio calculated by the model. In spite of those discrepancies, our study demonstrates that a high degree of compatibility is achieved between top-down pyrogenic and biogenic emissions derived by GOME-2 and OMI HCHO data, while the flux estimates are found to be weakly dependent to changes in key uncertain parameters in the performed sensitivity inversions.

This study identifies several important large regions where the differences between bottom-up and top-down estimates are particularly important and the inferred flux estimates from both satellites show a high degree of consistency, like the Amazon and the Southeast US. Recent airborne field measurements in those regions should provide additional constraints and help close the gap between bottom-up and top-down estimates. The increasing availability of in-situ observations of formaldehyde and related trace gases can provide a basis for improving and assessing model simulations of diurnal variations over a range of environmental conditions and interactions between biogenic and anthropogenic compounds (e.g. DiGangi et al., 2012). Furthermore, planned geostationary satellites have the potential to improve satellite based emission estimates by characterizing diurnal variations in atmospheric constituents (Saide et al., 2014). Finally, new cross section measurements of isoprene in the infrared open new avenues for the detection of isoprene using satellite (e.g. IASI) and a direct link to isoprene emission (Brauer et al., 2014).

Acknowledgements. This research was supported by the Belgian Science Policy Office through the PRODEX projects ACROSAT and IASI.Flow (2014–2015), and by the European Space Agency (ESA) through the GlobEmission project (2011–2016). P.-F. Coheur is senior research associate with FRS-FNRS.

ACPD
15, 12007–12067, 2015

References

Andreae, M. O. and Merlet, P.: Emission of trace gases and aerosols from biomass burning, Global Biogeochem. Cy., 15, 955–966, doi:10.1029/2000GB001382, 2001. 12014

Arneth, A., Schurgers, G., Lathiere, J., Duhl, T., Beerling, D. J., Hewitt, C. N., Martin, M., and Guenther, A.: Global terrestrial isoprene emission models: sensitivity to variability in climate and vegetation, Atmos. Chem. Phys., 11, 8037–8052, doi:10.5194/acp-11-8037-2011, 2011. 12011

Barkley, M. P., Palmer, P. I., Kuhn, U., Kesselmeier, J., Chance, K., Kurosu, T. P., Martin, R. V., Helmig, D., and Guenther, A.: Net ecosystem fluxes of isoprene over tropical South America inferred from Global Ozone Monitoring Experiment (GOME) observations of HCHO columns, J. Geophys. Res., 113, D20304, doi:10.1029/2008JD009863, 2008. 12032

Barkley, M. P., Palmer, P. I., De Smedt, I., Karl, T., Guenther, A., and Van Roozendael, M.: Regulated large-scale annual shutdown of Amazonian isoprene emissions?, Geophys. Res. Lett., 36, L04803, doi:10.1029/2008GL036843, 2009. 12011, 12032

Barkley, M. P., Palmer, P. I., Ganzeveld, L., Arneth, A., Hagberg, D., Karl, T., Guenther, A., Paulot, F., Wennberg, P. O., Mao, J., Kurosu, T. P., Chance, K., Müller, J.-F., De Smedt, I., Van Roozendael, M., Chen, D., Wang, Y., and Yantosca, R. M.: Can a "state of the art" chemistry transport model simulate Amazonian tropospheric chemistry?, J. Geophys. Res., 116, D16302, doi:10.1029/2011JD01589, 2011. 12019, 12036

Bloom, A. A., Worden, J., Jiang, Z., Worden, H., Kurosu, T., Frankenberg, C., and Schimel, D.: Remote sensing constraints on South America fire traits by Bayesian fusion of atmospheric and surface data, Geophys. Res. Lett., 42, 1268–1274, doi:10.1002/2014GL062584, 2015. 12031, 12037

Bloss, C., Wagner, V., Bonzanini, A., Jenkin, M. E., Wirtz, K., Martin-Reviejo, M., and Pilling, M. J.: Evaluation of detailed aromatic mechanisms (MCMv3 and MCMv3.1) against environmental chamber data, Atmos. Chem. Phys., 5, 623–639, doi:10.5194/acp-5-623-2005, 2005. 12015

Boersma, K. F., Eskes, H. J., Dirksen, R. J., van der A, R. J., Veefkind, J. P., Stammes, P., Huijnen, V., Kleipool, Q. L., Sneep, M., Claas, J., Leitão, J., Richter, A., Zhou, Y., and Brunner, D.: An improved tropospheric NO_2 column retrieval algorithm for the Ozone Monitoring Instrument, Atmos. Meas. Tech., 4, 1905–1928, doi:10.5194/amt-4-1905-2011, 2011. 12023

ACPD
15, 12007–12067, 2015

Brauer, C. S., Blake, T. A., Guenther, A. B., Sharpe, S. W., Sams, R. L., and Johnson, T. J.: Quantitative infrared absorption cross sections of isoprene for atmospheric measurements, Atmos. Meas. Tech., 7, 3839–3847, doi:10.5194/amt-7-3839-2014, 2014. 12038

Chance, K., Palmer, P. I., Spurr, R. J. D., Martin, R. V., Kurosu, T., and Jacob, D. J.: Satellite observations of formaldehyde over North America from GOME, Geophys. Res. Lett., 27, 3461–3464, 2000. 12011

Chang, D. and Song, Y.: Estimates of biomass burning emissions in tropical Asia based on satellite-derived data, Atmos. Chem. Phys., 10, 2335–2351, doi:10.5194/acp-10-2335-2010, 2010. 12033

Choi, W., Faloona, I. C., Bouvier-Brown, N. C., McKay, M., Goldstein, A. H., Mao, J., Brune, W. H., LaFranchi, B. W., Cohen, R. C., Wolfe, G. M., Thornton, J. A., Sonnenfroh, D. M., and Millet, D. B.: Observations of elevated formaldehyde over a forest canopy suggest missing sources from rapid oxidation of arboreal hydrocarbons, Atmos. Chem. Phys., 10, 8761–8781, doi:10.5194/acp-10-8761-2010, 2010. 12012

Crounse, J. D., Paulot, F., Kjaergaard, J. G., and Wennberg, P. O.: Peroxy radical isomerization in the oxidation of isoprene, Phys. Chem. Chem. Phys., 13, 13607–13613, 2011. 12015

Damian, V., Sandu, A., Damian, M., Potra, F., and Carmichael, G. R.: The Kinetic PreProcessor KPP – A Software Environment for Solving Chemical Kinetics, Comput. Chem. Eng., 26, 1567–1579, 2002. 12015

De Smedt, I., Van Roozendael, M., Stavrakou, T., Müller, J.-F., Lerot, C., Theys, N., Valks, P., Hao, N., and van der A, R.: Improved retrieval of global tropospheric formaldehyde columns from GOME-2/MetOp-A addressing noise reduction and instrumental degradation issues, Atmos. Meas. Tech., 5, 2933–2949, doi:10.5194/amt-5-2933-2012, 2012. 12012, 12022

De Smedt, I., Stavrakou, T., Hendrick, F., Danckaert, T., Vlemmix, T., Pinardi, G., Theys, N., Lerot, C., Müller, J.-F., Veefkind, P., and Van Roozendael, M.: Diurnal, seasonal and long-term variations of global formaldehyde columns inferred from combined OMI and GOME-2 observations, Atmos. Chem. Phys. Discuss., accepted, 2015. 12012, 12020, 12022, 12023, 12028

DiGangi, J. P., Henry, S. B., Kammrath, A., Boyle, E. S., Kaser, L., Schnitzhofer, R., Graus, M., Turnipseed, A., Park, J-H., Weber, R. J., Hornbrook, R. S., Cantrell, C. A., Maudlin III, R. L., Kim, S., Nakashima, Y., Wolfe, G. M., Kajii, Y., Apel, E.C., Goldstein, A. H., Guenther, A., Karl, T., Hansel, A., and Keutsch, F. N.: Observations of glyoxal and formaldehyde as metrics

ACPD
15, 12007–12067, 2015

for the anthropogenic impact on rural photochemistry, Atmos. Chem. Phys., 12, 9529–9543, doi:10.5194/acp-12-9529-2012, 2012. 12038

Dufour, G., Wittrock, F., Camredon, M., Beekmann, M., Richter, A., Aumont, B., and Burrows, J. P.: SCIAMACHY formaldehyde observations: constraint for isoprene emission estimates over Europe?, Atmos. Chem. Phys., 9, 1647–1664, doi:10.5194/acp-9-1647-2009, 2009. 12011

Fried, A., Walega, J. G., Olson, J. R., Crawford, J. H., Chen, G., Weibring, P., Richter, D., Roller, C., Tittel, F., Heikes, B. G., Snow, J. A., Shen, H., O'Sullivan, D. W., Porter, M. J., Fuelberg, H. E., Halland, J. J., and Millet, D. B.: Formaldehyde over North America and the North Atlantic during the summer 2004 INTEX campaign: methods, observed distributions and measurement comparisons, J. Geophys. Res., 113, D10302, doi:10.1029/2007JD009185, 2008. 12027

George, M., Clerbaux, C., Hurtmans, D., Turquety, S., Coheur, P.-F., Pommier, M., Hadji-Lazaro, J., Edwards, D. P., Worden, H., Luo, M., Rinsland, C., and McMillan, W.: Carbon monoxide distributions from the IASI/METOP mission: evaluation with other space-borne remote sensors, Atmos. Chem. Phys., 9, 8317–8330, doi:10.5194/acp-9-8317-2009, 2009. 12031

Gielen, C., Van Roozendael, M., Hendrick, F., Pinardi, G., Vlemmix, T., De Bock, V., De Backer, H., Fayt, C., Hermans, C., Gillotay, D., and Wang, P.: A simple and versatile cloud-screening method for MAX-DOAS retrievals, Atmos. Meas. Tech., 7, 3509–3527, doi:10.5194/amt-7-3509-2014, 2014. 12020

González Abad, G., Liu, X., Chance, K., Wang, H., Kurosu, T. P., and Suleiman, R.: Updated Smithsonian Astrophysical Observatory Ozone Monitoring Instrument (SAO OMI) formaldehyde retrieval, Atmos. Meas. Tech., 8, 19–32, doi:10.5194/amt-8-19-2015, 2015. 12012

Goodwin, J. W. L., Salway, A. G., Murrells, T. P., Dore, C. J., Passant, N. R., King, K. R., Coleman, P. J., Hobson, M. M., Pye, S. T., and Watterson, J. D.: UK Emissions of air pollutants 1970–1999, National Atmospheric Emissions Inventory Report, AEAT/ENV/R/0798, ISBN 1-85580-031 4, 2001. 12015, 12049

Griffiths, P. R. and de Haseth, J. A: Fourier Transform Infrared Spectrometry, John Wiley & Sons, Inc., Hoboke, NJ, 2007. 12021

Guenther, A., Karl, T., Harley, P., Wiedinmyer, C., Palmer, P. I., and Geron, C.: Estimates of global terrestrial isoprene emissions using MEGAN (Model of Emissions of Gases and

ACPD
15, 12007–12067, 2015

Aerosols from Nature), Atmos. Chem. Phys., 6, 3181–3210, doi:10.5194/acp-6-3181-2006, 2006. 12011, 12029

Guenther, A. B., Jiang, X., Heald, C. L., Sakulyanontvittaya, T., Duhl, T., Emmons, L. K., and Wang, X.: The Model of Emissions of Gases and Aerosols from Nature version 2.1 (MEGAN2.1): an extended and updated framework for modeling biogenic emissions, Geosci. Model Dev., 5, 1471–1492, doi:10.5194/gmd-5-1471-2012, 2012. 12029

Hendrick, F., Müller, J.-F., Clémer, K., Wang, P., De Mazière, M., Fayt, C., Gielen, C., Hermans, C., Ma, J. Z., Pinardi, G., Stavrakou, T., Vlemmix, T., and Van Roozendael, M.: Four years of ground-based MAX-DOAS observations of HONO and NO_2 in the Beijing area, Atmos. Chem. Phys., 14, 765–781, doi:10.5194/acp-14-765-2014, 2014. 12020

Hewson, W., Bösch, H., Barkley, M. P., and De Smedt, I.: Characterisation of GOME-2 formaldehyde retrieval sensitivity, Atmos. Meas. Tech., 6, 371–386, doi:10.5194/amt-6-371-2013, 2013. 12012

Hönninger, G., von Friedeburg, C., and Platt, U.: Multi axis differential optical absorption spectroscopy (MAX-DOAS), Atmos. Chem. Phys., 4, 231–254, doi:10.5194/acp-4-231-2004, 2004. 12021

Huang, X., Xi, M., Li, J., and Song, Y.: A high-resolution emission inveotry of crop burning in fields in China based on MODIS thermal anomalies/fire products, Atmos. Environ., 50, 9–15, 2012. 12030

Jenkin, M. E., Murrels, T. P., and Passant, N. R.: The temporal dependence of ozone precursor emissions: estimation and application, Report No. AEAT/R/ENV/0355 Issue 1, AEA Technology, Harwell, 2000. 12013

Junkermann, W.: On the distribution of formaldehyde in the western Po-Valley, Italy, during FORMAT 2002/2003, Atmos. Chem. Phys., 9, 9187–9196, doi:10.5194/acp-9-9187-2009, 2009. 12012

Kleipool, Q. L., Dobber, M. R., de Haan, J. F., and Levelt, P. F.: Earth surface reflectance climatology from 3 years of OMI data, J. Geophys. Res., 113, D18308, doi:10.1029/2008JD010290, 2008. 12023

Konovalov, I. B., Beekmann, M., Kuznetsova, I. N., Yurova, A., and Zvyagintsev, A. M.: Atmospheric impacts of the 2010 Russian wildfires: integrating modelling and measurements of an extreme air pollution episode in the Moscow region, Atmos. Chem. Phys., 11, 10031–10056, doi:10.5194/acp-11-10031-2011, 2011. 12028

ACPD
15, 12007–12067, 2015

Krol, M., Peters, W., Hooghiemstra, P., George, M., Clerbaux, C., Hurtmans, D., McInerney, D., Sedano, F., Bergamaschi, P., El Hajj, M., Kaiser, J. W., Fisher, D., Yershov, V., and Muller, J.-P.: How much CO was emitted by the 2010 fires around Moscow?, Atmos. Chem. Phys., 13, 4737–4747, doi:10.5194/acp-13-4737-2013, 2013. 12028

Kurokawa, J., Ohara, T., Morikawa, T., Hanayama, S., Janssens-Maenhout, G., Fukui, T., Kawashima, K., and Akimoto, H.: Emissions of air pollutants and greenhouse gases over Asian regions during 2000–2008: Regional Emission inventory in ASia (REAS) version 2, Atmos. Chem. Phys., 13, 11019–11058, doi:10.5194/acp-13-11019-2013, 2013. 12013, 12029

Langford, B., Misztal, P. K., Nemitz, E., Davison, B., Helfter, C., Pugh, T. A. M., MacKenzie, A. R., Lim, S. F., and Hewitt, C. N.: Fluxes and concentrations of volatile organic compounds from a South-East Asian tropical rainforest, Atmos. Chem. Phys., 10, 8391–8412, doi:10.5194/acp-10-8391-2010, 2010. 12032

Logan, J. A., Prather, M. J., Wofsy, S. C., and McElroy, M. B.: Tropospheric chemistry: a global perspective, J. Geophys. Res., 86, 7210–7254, 1981. 12019

MacDonald, S. M., Oetjen, H., Mahajan, A. S., Whalley, L. K., Edwards, P. M., Heard, D. E., Jones, C. E., and Plane, J. M. C.: DOAS measurements of formaldehyde and glyoxal above a south-east Asian tropical rainforest, Atmos. Chem. Phys., 12, 5949–5962, doi:10.5194/acp-12-5949-2012, 2012. 12012

Marais, E. A., Jacob, D. J., Kurosu, T. P., Chance, K., Murphy, J. G., Reeves, C., Mills, G., Casadio, S., Millet, D. B., Barkley, M. P., Paulot, F., and Mao, J.: Isoprene emissions in Africa inferred from OMI observations of formaldehyde columns, Atmos. Chem. Phys., 12, 6219–6235, doi:10.5194/acp-12-6219-2012, 2012. 12011, 12034

Marais, E. A., Jacob, D. J., Guenther, A., Chance, K., Kurosu, T. P., Murphy, J. G., Reeves, C. E., and Pye, H. O. T.: Improved model of isoprene emissions in Africa using Ozone Monitoring Instrument (OMI) satellite observations of formaldehyde: implications for oxidants and particulate matter, Atmos. Chem. Phys., 14, 7693–7703, doi:10.5194/acp-14-7693-2014, 2014. 12011

Marengo, J. A., Nobre, C., Tomasella, J., Oyama, M., Sampaio de Oliveira, G., de Oliveira, R., Camargo, H., Alves, L., and Brown, I. F.: The drought of Amazonia in 2005, J. Climate, 21, 495–516, doi:10.1175/2007JCLI1600.1, 2008. 12030

Marengo, J. A., Tomasella, J., Alves, L. M., Soares, W. R., and Rodriguez, D. A.: The drought of 2010 in the context of historical droughts in the Amazon region, Geophys. Res. Lett., 38, L12703, doi:10.1029/2011GL047436, 2011. 12030

ACPD
15, 12007–12067, 2015

Martin, R. V, Chance, K. V., Jacob, D. J., Kurosu, T. P., Spurr, R. J. D., Bucsela, E. J., Gleason, J., Palmer, P. I., Bey, I., Fiore, A. M., Li, Q., Yantosca, R. M., and Koelemeijer, R. B. A.: An improved retrieval of tropospheric nitrogen dioxide from GOME, J. Geophys. Res., 107, 4437, doi:10.1029/2001JD001027, 2002. 12023

Millet, D. B., Jacob, D. J., Turquety, S., Hudman, R. C., Wu, S., Fried, A., Walega, J., Heikes, B. G., Blake, D. R., Singh, H. B., Anderson, B. E., and Clarke, A. D.: Formaldehyde distribution over North America: implications for satellite retrievals of formaldehyde columns and isoprene emission, J. Geophys. Res., 111, D24S02, doi:10.1029/2005JD006853, 2006. 12011

Millet, D. B., Jacob, D. J., Boersma, K. F., Fu, T., Kurosu, T. P., Chance, K., Heald, C. L., and Guenther, A.: Spatial distribution of isoprene emissions from North America derived from formaldehyde columns measurements by the OMI satellite sensor, J. Geophys. Res., 113, D02307, doi:10.1029/2007JD008950, 2008. 12011, 12027

Müller, J.-F. and Stavrakou, T.: Inversion of CO and NO_x emissions using the adjoint of the IMAGES model, Atmos. Chem. Phys., 5, 1157–1186, doi:10.5194/acp-5-1157-2005, 2005. 12012

Müller, J.-F., Stavrakou, T., Wallens, S., De Smedt, I., Van Roozendael, M., Potosnak, M. J., Rinne, J., Munger, B., Goldstein, A., and Guenther, A. B.: Global isoprene emissions estimated using MEGAN, ECMWF analyses and a detailed canopy environment model, Atmos. Chem. Phys., 8, 1329–1341, doi:10.5194/acp-8-1329-2008, 2008. 12014

Palmer, P. I., Jacob, D. J., Fiore, A., Martin, R. V., Chance, K. V., Kurosu, T. P., Bey, I., and Yantosca, R.: Air mass factor formulation for spectroscopic measurements from satellites: application to formaldehyde retrievals from the Global Ozone Monitoring Experiment, J. Geophys. Res., 106, 14539–14550, doi:10.1029/2000JD900772, 2001. 12023

Palmer, P. I., Jacob, D. J., Fiore, A., Chance, K. V., Martin, R. V., Kurosu, T. P., Bey, I., Yantosca, R., Fiore, A., and Li, Q.: Mapping isoprene emissions over North America using formaldehyde column observations from space, J. Geophys. Res., 108, 4180, doi:10.1029/2002JD002153, 2003. 12011, 12027

Palmer, Abbot, P. I. D. S., Fu, T.-M., Jacob, D. J., Chance, K., Kurosu, T. P., Guenther, A., Wiedinmyer, C., Stanton, J. C., Pilling, M. J., Pressley, S. N., Lamb, B., and Sumner, A. L.: Quantifying the seasonal and interannual variability of North American isoprene emissions using satellite observations of the formaldehyde column, J. Geophys. Res., 111, D12315, doi:10.1029/2005JD006689, 2006. 12011

ACPD
15, 12007–12067, 2015

Peeters, J. and Müller, J.-F.: HO_x radical regeneration in isoprene oxidation via peroxy radical isomerisations. II: Experimental evidence and global impact, Phys. Chem. Chem. Phys., 12, 14227–14235, doi:10.1039/C0CP00811G, 2010. 12014

Peeters, J., Nguyen, T. L., and Vereecken, L.: HO_x radical regeneration in the oxidation of isoprene, Phys. Chem. Chem. Phys., 11, 5935–5939, 2009. 12014

Peeters, J., Müller, J.-F., Stavrakou, T., and Nguyen, S. V.: Hydroxyl radical recycling in isoprene oxidation driven by hydrogen bonding and hydrogen tunneling: the upgraded LIM1 mechanism, J. Phys. Chem. A, 118, 8625–8643, doi:10.1021/jp5033146, 2014. 12014

Peters, E., Wittrock, F., Großmann, K., Frieß, U., Richter, A., and Burrows, J. P.: Formaldehyde and nitrogen dioxide over the remote western Pacific Ocean: SCIAMACHY and GOME-2 validation using ship-based MAX-DOAS observations, Atmos. Chem. Phys., 12, 11179–11197, doi:10.5194/acp-12-11179-2012, 2012. 12012

Pinardi, G., Van Roozendael, M., Abuhassan, N., Adams, C., Cede, A., Clémer, K., Fayt, C., Frieß, U., Gil, M., Herman, J., Hermans, C., Hendrick, F., Irie, H., Merlaud, A., Navarro Comas, M., Peters, E., Piters, A. J. M., Puentedura, O., Richter, A., Schönhardt, A., Shaiganfar, R., Spinei, E., Strong, K., Takashima, H., Vrekoussis, M., Wagner, T., Wittrock, F., and Yilmaz, S.: MAX-DOAS formaldehyde slant column measurements during CINDI: intercomparison and analysis improvement, Atmos. Meas. Tech., 6, 167–185, doi:10.5194/amt-6-167-2013, 2013. 12020

Platt, U. and Stutz, J.: Differential Absorption Spectroscopy, Physics of Earth and Space Environments, Springer-Verlag, Berlin Heidelberg, doi:10.1007/978-3-540-75776-4, 2008. 12021

R'Honi, Y., Clarisse, L., Clerbaux, C., Hurtmans, D., Duflot, V., Turquety, S., Ngadi, Y., and Coheur, P.-F.: Exceptional emissions of NH_3 and HCOOH in the 2010 Russian wildfires, Atmos. Chem. Phys., 13, 4171–4181, doi:10.5194/acp-13-4171-2013, 2013. 12028

Richter, A., Begoin, M., Hilboll, A., and Burrows, J. P.: An improved NO_2 retrieval for the GOME-2 satellite instrument, Atmos. Meas. Tech., 4, 1147–1159, doi:10.5194/amt-4-1147-2011, 2011. 12022

Roberts, G., Wooster, M. J., and Lagoudakis, E.: Annual and diurnal african biomass burning temporal dynamics, Biogeosciences, 6, 849–866, doi:10.5194/bg-6-849-2009, 2009. 12014

Saide, P. E., Kim, J., Song, C. H., Choi, M., Cheng, Y., and Carmichael, G. R.: Assimilation of next generation geostationary aerosol optical depth retrievals to improve air quality simulations, Geophys. Res. Lett., 41, 9188–9196, doi:10.1002/2014GL062089, 2014. 12038

ACPD
15, 12007–12067, 2015

Sander, S. P., Abbatt, J., Barker, J. R., Burkholder, J. B., Friedl, R. R., Golden, D. M., Huie, R. E., Kolb, C. E., Kurylo, M. J., Moortgat, G. K., Orkin, V. L., and Wine, P. H.: Chemical Kinetics and Photochemical Data for Use in Atmospheric Studies, Evaluation No. 17, JPL Publication 10-6, Jet Propulsion Laboratory, Pasadena, available at: http://jpldataeval.jpl.nasa.gov (last access: 20 April 2015), 2011. 12010

Saunders, S. M., Jenkin, M. E., Derwent, R. G., and Pilling, M. J.: Protocol for the development of the Master Chemical Mechanism, MCM v3 (Part A): tropospheric degradation of non-aromatic volatile organic compounds, Atmos. Chem. Phys., 3, 161–180, doi:10.5194/acp-3-161-2003, 2003. 12015

Schultz, M. G, Heil, A., Hoelzemann, J. J., Spessa, A., Thonicke, K., Goldammer, J., Held, A. C., and Pereira, J. M.: Global Emissions from Wildland Fires from 1960 to 2000, Global Biogeochem. Cy., 22, GB2002, doi:10.1029/2007GB003031, 2008. 12013

Singh, H. B., Brune, W. H., Crawford, J. H., Jacob, D. J., and Russell, P. B.: Overview of the summer 2004 Intercontinental Chemical Transport Experiment North America (INTEX-A), J. Geophys. Res., 111, D24S01, doi:10.1029/2006JD007905, 2006. 12027

Sofiev, M., Ermakova, T., and Vankevich, R.: Evaluation of the smoke-injection height from wildland fires using remote-sensing data, Atmos. Chem. Phys., 12, 1995–2006, doi:10.5194/acp-12-1995-2012, 2012. 12014

Sofiev, M., Vankevich, R., Ermakova, T., and Hakkarainen, J.: Global mapping of maximum emission heights and resulting vertical profiles of wildfire emissions, Atmos. Chem. Phys., 13, 7039–7052, doi:10.5194/acp-13-7039-2013, 2013. 12014

Spurr, R. J. D.: LIDORT and VLIDORT: linearized pseudo-spherical scalar and vector discrete ordinate radiative transfer models for use in remote sensing retrieval problems, in: Light Scattering Reviews, edited by: Kokhanovsky, A., Springer Praxis Books, Berlin, 229–271, 2008. 12023

Stammes, P., Sneep, M., de Haan, J. F., Veefkind, J. P., Wang, P., and Levelt, P. F.: Effective cloud fractions from the Ozone Monitoring Instrument: theoretical framework and validation, J. Geophys. Res., 113, D16S38, doi:10.1029/2007JD008820, 2008. 12023

Stavrakou, T., Müller, J.-F., De Smedt, I., Van Roozendael, M., van der Werf, G. R., Giglio, L., and Guenther, A.: Evaluating the performance of pyrogenic and biogenic emission inventories against one decade of space-based formaldehyde columns, Atmos. Chem. Phys., 9, 1037–1060, doi:10.5194/acp-9-1037-2009, 2009a. 12010, 12011, 12012, 12013, 12025

ACPD
15, 12007–12067, 2015

Stavrakou, T., Müller, J.-F., De Smedt, I., Van Roozendael, M., van der Werf, G. R., Giglio, L., and Guenther, A.: Global emissions of non-methane hydrocarbons deduced from SCIAMACHY formaldehyde columns through 2003–2006, Atmos. Chem. Phys., 9, 3663–3679, doi:10.5194/acp-9-3663-2009, 2009b. 12011, 12024, 12027, 12031, 12032, 12035

Stavrakou, T., Peeters, J., and Müller, J.-F.: Improved global modelling of HO_x recycling in isoprene oxidation: evaluation against the GABRIEL and INTEX-A aircraft campaign measurements, Atmos. Chem. Phys., 10, 9863–9878, doi:10.5194/acp-10-9863-2010, 2010. 12014

Stavrakou, T., Müller, J.-F., Boersma, K. F., van der A, R. J., Kurokawa, J., Ohara, T., and Zhang, Q.: Key chemical NO_x sink uncertainties and how they influence top-down emissions of nitrogen oxides, Atmos. Chem. Phys., 13, 9057–9082, doi:10.5194/acp-13-9057-2013, 2013. 12013

Stavrakou, T., Müller, J.-F., Bauwens, M., De Smedt, I., Van Roozendael, M., Guenther, A., Wild, M., and Xia, X.: Isoprene emissions over Asia 1979–2012: impact of climate and land-use changes, Atmos. Chem. Phys., 14, 4587–4605, doi:10.5194/acp-14-4587-2014, 2014. 12014, 12029, 12032

Takahashi, H. G., Fujinami, H., Yasunari, T., and Matsumoto, J.: Diurnal rainfall pattern observed by Tropical Rainfall Measuring Mission Precipitation Radar (TRMM-PR) around the Indochina peninsula, J. Geophys. Res., 115, D07109, doi:10.1029/2009JD012155, 2010. 12034

Valks, P., Pinardi, G., Richter, A., Lambert, J.-C., Hao, N., Loyola, D., Van Roozendael, M., and Emmadi, S.: Operational total and tropospheric NO_2 column retrieval for GOME-2, Atmos. Meas. Tech., 4, 1491–1514, doi:10.5194/amt-4-1491-2011, 2011. 12020

van der Werf, G. R., Randerson, J. T., Giglio, L., Collatz, G. J., Mu, M., Kasibhatla, P. S., Morton, D. C., DeFries, R. S., Jin, Y., and van Leeuwen, T. T.: Global fire emissions and the contribution of deforestation, savanna, forest, agricultural, and peat fires (1997–2009), Atmos. Chem. Phys., 10, 11707–11735, doi:10.5194/acp-10-11707-2010, 2010. 12014

Vigouroux, C., Hendrick, F., Stavrakou, T., Dils, B., De Smedt, I., Hermans, C., Merlaud, A., Scolas, F., Senten, C., Vanhaelewyn, G., Fally, S., Carleer, M., Metzger, J.-M., Müller, J.-F., Van Roozendael, M., and De Mazière, M.: Ground-based FTIR and MAX-DOAS observations of formaldehyde at Réunion Island and comparisons with satellite and model data, Atmos. Chem. Phys., 9, 15891–15957, doi:10.5194/acp-9-9523-2009, 2009. 12021

Vlemmix, T., Hendrick, F., Pinardi, G., De Smedt, I., Fayt, C., Hermans, C., Piters, A., Wang, P., Levelt, P., and Van Roozendael, M.: MAX-DOAS observations of aerosols, formaldehyde and

ACPD
15, 12007–12067, 2015

nitrogen dioxide in the Beijing area: comparison of two profile retrieval approaches, Atmos. Meas. Tech., 8, 941–963, doi:10.5194/amt-8-941-2015, 2015. 12020

Wang, P., Stammes, P., van der A, R., Pinardi, G., and van Roozendael, M.: FRESCO+: an improved O_2 A-band cloud retrieval algorithm for tropospheric trace gas retrievals, Atmos. Chem. Phys., 8, 6565–6576, doi:10.5194/acp-8-6565-2008, 2008. 12023

Wiedinmyer, C., Akagi, S. K., Yokelson, R. J., Emmons, L. K., Al-Saadi, J. A., Orlando, J. J., and Soja, A. J.: The Fire INventory from NCAR (FINN): a high resolution global model to estimate the emissions from open burning, Geosci. Model Dev., 4, 625–641, doi:10.5194/gmd-4-625-2011, 2011. 12033

Yamaji, K., Li, J., Uno, I., Kanaya, Y., Irie, H., Takigawa, M., Komazaki, Y., Pochanart, P., Liu, Y., Tanimoto, H., Ohara, T., Yan, X., Wang, Z., and Akimoto, H.: Impact of open crop residual burning on air quality over Central Eastern China during the Mount Tai Experiment 2006 (MTX2006), Atmos. Chem. Phys., 10, 7353–7368, doi:10.5194/acp-10-7353-2010, 2010. 12030

Yurganov, L. N., Rakitin, V., Dzhola, A., August, T., Fokeeva, E., George, M., Gorchakov, G., Grechko, E., Hannon, S., Karpov, A., Ott, L., Semutnikova, E., Shumsky, R., and Strow, L.: Satellite- and ground-based CO total column observations over 2010 Russian fires: accuracy of top-down estimates based on thermal IR satellite data, Atmos. Chem. Phys., 11, 7925–7942, doi:10.5194/acp-11-7925-2011, 2011. 12028

ACPD
15, 12007–12067, 2015

Table 1. MCMv3.2-based short-term yields (after 1 day) and final yields (after 60 days) of HCHO from the oxidation of NMVOCs not explicitly considered in the IMAGES mechanism. The OH-reaction rates at 298 K and the estimated emissions for the UK (Goodwin et al., 2001) are also provided.

	NMVOC	Molecular weight	Y_{1d} mol mol^{-1}	Y_{60d} mol mol^{-1}	OH-reaction rate cm^3 molec^{-1} s^{-1}	Emission kt yr^{-1}
Higher alkanes	butane	58	0.280	2.033	2.35×10^{-12}	151.11
	pentane	72	0.600	2.098	4.00×10^{-12}	64.53
	hexane	86	0.624	2.805	5.45×10^{-12}	51.46
	heptane	100	0.520	2.952	7.02×10^{-12}	22.49
	octane	114	0.505	2.976	8.70×10^{-12}	15.08
	nonane	128	0.541	3.128	9.98×10^{-12}	6.03
	decane	142	0.607	3.826	1.12×10^{-11}	11.04
	undecane	156	0.717	4.339	1.29×10^{-11}	4.87
	2-methylpropane	58	0.308	2.710	2.18×10^{-12}	40.92
	2-methylbutane	72	0.361	2.810	3.70×10^{-12}	70.18
	2-methylpentane	86	0.530	2.914	5.30×10^{-12}	5.73
	3-methylpentane	86	0.683	2.994	5.40×10^{-12}	3.96
	2-methylhexane	100	0.525	3.814	6.86×10^{-12}	5.36
	3-methylhexane	100	0.670	3.283	7.15×10^{-12}	4.38
	cyclohexane	86	0.541	1.615	7.20×10^{-12}	4.31
Higher alkenes	1-butene	56	1.790	1.911	3.14×10^{-11}	4.15
	2-methylpropene	56	1.117	2.890	5.11×10^{-11}	11.37
	1-pentene	70	1.852	2.157	3.14×10^{-11}	3.81
	1.3-butadiene	54	1.644	1.711	6.65×10^{-11}	6.19
Higher aromatics	ethylbenzene	106	0.533	1.111	7.00×10^{-12}	18.48
	1.2.3-trimethylbenzene	120	2.883	3.189	3.27×10^{-11}	5.01
	1.2.4-trimethylbenzene	120	2.758	2.999	3.25×10^{-11}	18.45
	1.3.5-trimethylbenzene	120	2.554	2.969	5.67×10^{-11}	6.75
	styrene	104	0.942	0.987	5.80×10^{-11}	4.14
Others	1-propanol	60	0.949	1.476	5.82×10^{-12}	4.79
	2-propanol	60	0.192	1.935	5.09×10^{-12}	8.44
	1-butanol	74	1.166	1.728	8.48×10^{-12}	5.63
	2-butanol	74	0.683	2.099	8.70×10^{-12}	4.05
	methyl acetate	74	0.115	1.661	3.49×10^{-13}	4.66
	ethyl acetate	88	0.462	1.823	1.68×10^{-12}	13.72
	butyl acetate	116	0.615	2.469	4.92×10^{-12}	6.88
	4-methyl-2-pentanone	100	1.770	3.759	1.41×10^{-11}	11.73

ACPD
15, 12007–12067, 2015

Table 2. Performed emission inversions.

Name	Description
GOME-2	Use GOME-2 data
OMI	Use OMI data
OMI-DE	Doubled a priori errors on the emission fluxes
OMI-HE	Halved a priori errors on the emission fluxes
OMI-CF	Use only OMI data with cloud fraction < 0.2
OMI-IS	Ignore isomerization of isoprene peroxy radicals

ACPD
15, 12007–12067, 2015

Table 3. A priori and top-down VOC emissions (Tg yr^{-1}) by region. The emission inversions are defined in Table 2. The regions are defined as follows. North America: US and Canada, Southern America: Mexico, Central and South America, Northern (Southern) Africa: north (south) of the equator, Tropics: 25° S–25° N, Southeastern US: 25–38° N, 60–100° W, Amazonia: 14° S–10° N, 45–80° W, Indonesia: 10° S–6° N, 95–142.5° E, Indochina: 6–22° N, 97.5–110° E, Europe extends to Urals (55° E), FSU = Former Soviet Union.

Biomass burning (Tg VOC yr^{-1})	A priori	GOME-2	OMI	OMI-DE	OMI-HE	OMI-CF	OMI-IS
North America	5.3	3.6	3.3	5.3	2.9	4.6	3.2
Southern America	36.9	20.7	17.1	16.8	17.8	16.4	16.2
Amazonia	26.5	13.0	10.4	10.2	10.8	10.0	9.7
Northern Africa	14.9	8.6	8.8	8.8	9.2	9.7	8.1
Southern Africa	25.8	17.6	23.8	24.6	23.0	25.5	23.1
Indochina	6.2	4.6	5.3	5.6	4.7	5.6	5.0
Tropics	93.3	56.8	60.6	61.6	60.4	63.0	57.8
Extratropics	12.0	10.0	9.9	13.4	8.8	12.1	9.2
Global	105.4	67.0	70.5	74.9	69.1	75.1	67.1
Isoprene (Tg yr^{-1})	A priori	GOME-2	OMI	OMI-DE	OMI-HE	OMI-CF	OMI-IS
Europe (excl. FSU)	3.8	3.3	3.8	3.7	3.4	3.9	3.7
Europe	7.4	6.9	8.2	8.8	7.7	8.6	8.1
North America	34.7	26.5	29.9	28.0	31.9	30.4	28.6
Southeastern US	14.5	8.9	10.8	9.8	12.2	11.3	9.9
Southern America	149.5	142.1	121.2	115.9	128.9	125.6	114.0
Amazonia	99.4	92.5	73.7	69.1	80.6	77.2	67.9
Northern Africa	50.6	45.3	43.7	40.4	46.8	44.7	41.5
Southern Africa	31.0	31.3	31.5	32.8	31.0	34.2	30.7
Indonesia	11.6	10.3	11.1	10.5	11.4	10.6	10.9
Indochina	7.6	7.1	7.5	7.3	7.5	7.4	7.3
Tropics	314.8	291.1	272.3	261.9	286.2	281.3	260.2
Extratropics	48.3	39.4	44.7	44.1	45.8	46.4	43.3
Global	363.1	330.5	317.0	305.9	332.1	327.8	303.5
Anthropogenic (Tg VOC yr^{-1})	A priori	GOME-2	OMI	OMI-DE	OMI-HE	OMI-CF	OMI-IS
Global	155.6	138.6	157.5	162.0	154.2	163.4	155.8

ACPD
15, 12007–12067, 2015

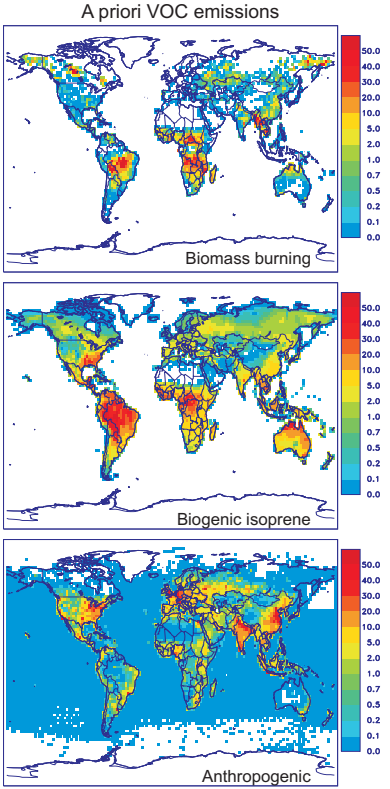

Figure 1. A priori annually averaged pyrogenic NMVOC, biogenic isoprene and anthropogenic NMVOC emissions used in the CTM. Units are 10^{10} molec cm^{-2} s^{-1}.

ACPD
15, 12007–12067, 2015

Hydrocarbon emissions derived from GOME-2 and OMI HCHO columns

T. Stavrakou et al.

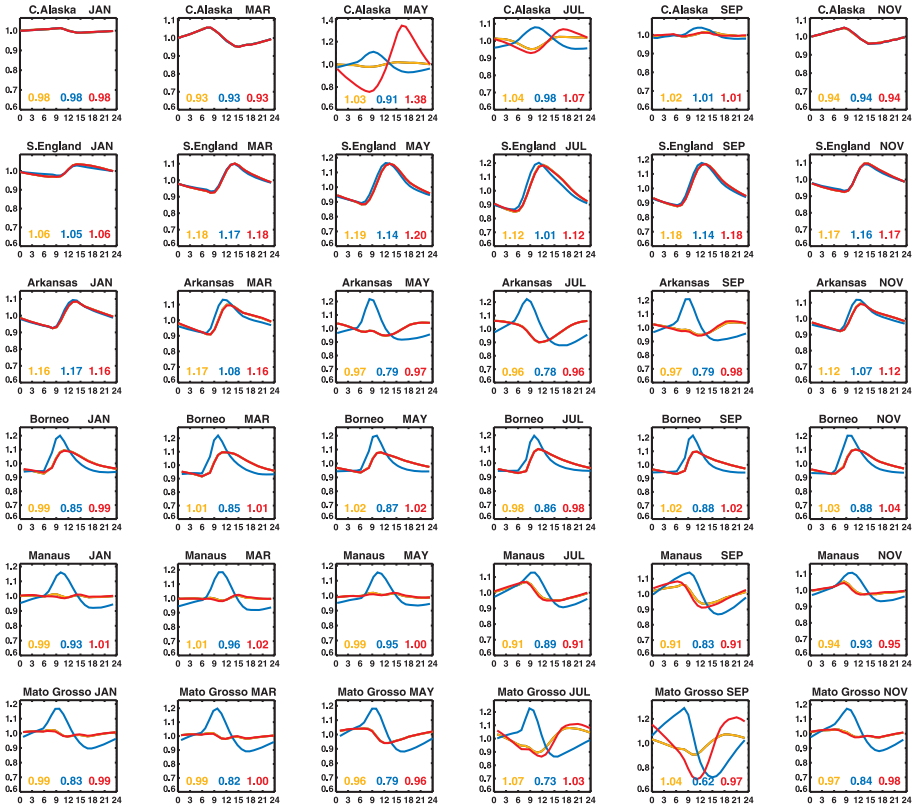

Figure 2. Modelled diurnal variations of HCHO columns (normalized at noon) at six locations, Central Alaska (65° N, 151° W), South England (51° N, 2.5° W), Arkansas (35° N, 91° W), Borneo (4° N, 117° E), Manaus (3° S, 61° W), and Mato Grosso (9° S, 51° W) in January, March, May, July, September and November 2010. The curves represent the standard simulation (in red), a simulation without biomass burning emissions (in orange) and a simulation ignoring the diurnal variation of emissions (in blue). The modelled ratios of 13:30 to 09:30 LT columns are given inside each panel.

ACPD
15, 12007–12067, 2015

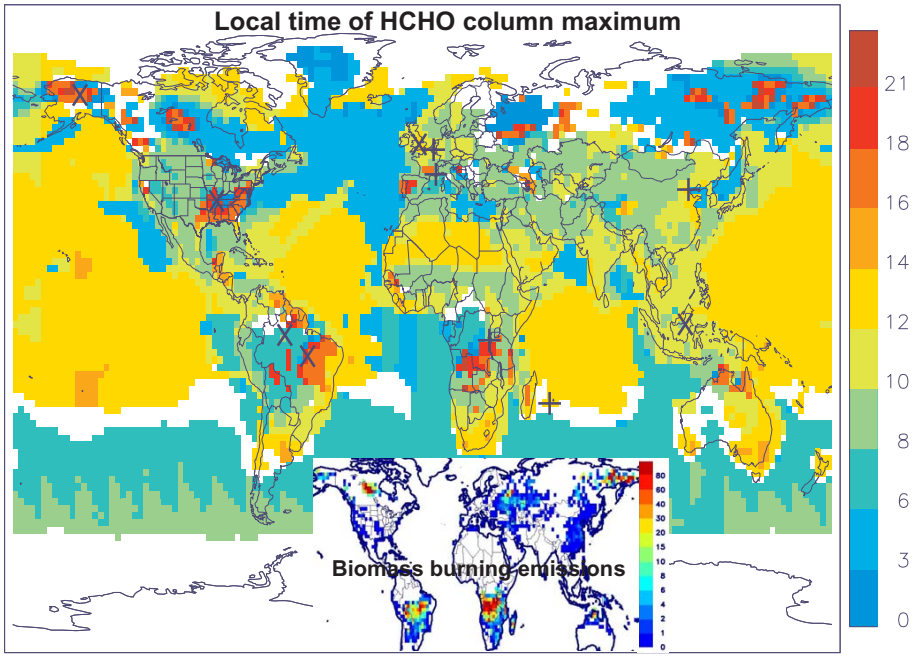

Figure 3. Modelled local time (in hour) of the maximum in HCHO column, for July 2010. The locations of sites for which comparisons are shown in Figs. 2, 4 and 5 are shown as crosses (x) and plus symbols (+), respectively. White color represents regions with diurnal variability of less than 5 %. The distribution of open fire NMVOC emissions (10^{10} molec cm^{-2} s^{-1}) for the same month is also shown inset.

ACPD
15, 12007–12067, 2015

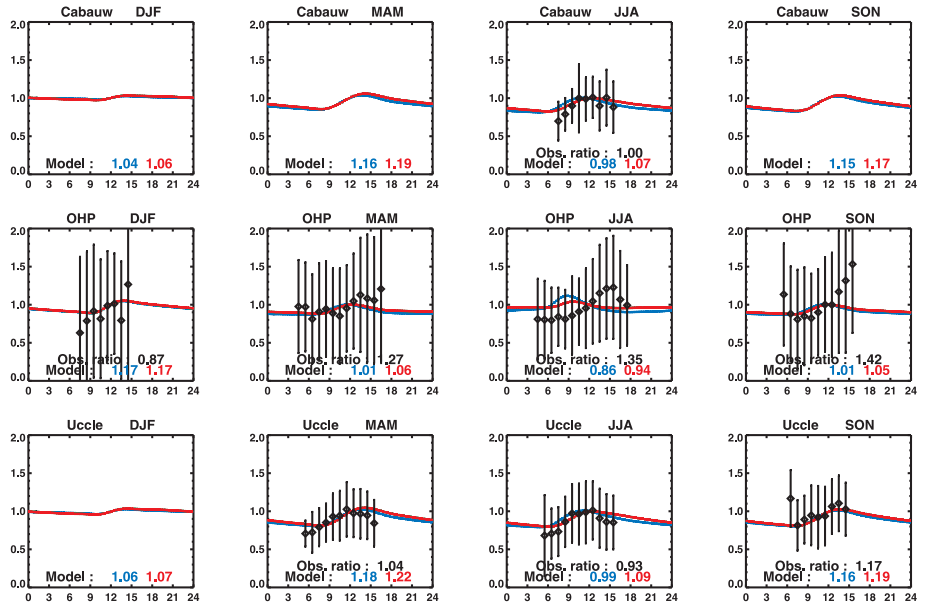

Figure 4. Seasonally averaged observed (black) and modelled (red) diurnal variations of HCHO columns at 3 European sites, Cabauw, Observatoire de Haute Provence, and Uccle. The observed columns are obtained using the MAX-DOAS technique (Sect. 3). The errors bars correspond to the measurement standard deviation. Modelled columns calculated assuming no diurnal emission variability are shown in blue. The observed and modelled ratios (blue and red) of 13:30 to 09:30 LT columns are given inset.

ACPD
15, 12007–12067, 2015

Hydrocarbon emissions derived from GOME-2 and OMI HCHO columns

T. Stavrakou et al.

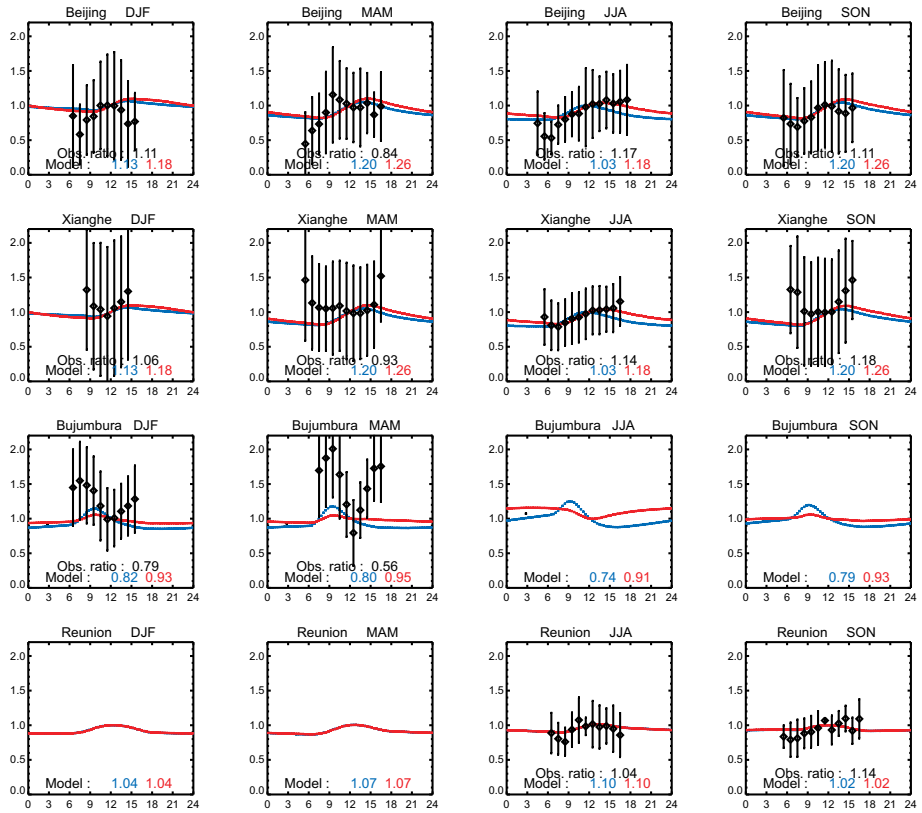

Figure 5. As in Fig. 4, comparison between modelled and observed diurnal variations for four sites: Beijing, Xianghe, Bujumbura and Reunion Island. The observations were obtained using the MAX-DOAS (Beijing, Xianghe, Bujumbura) and FTIR (Reunion Island) techniques.

ACPD
15, 12007–12067, 2015

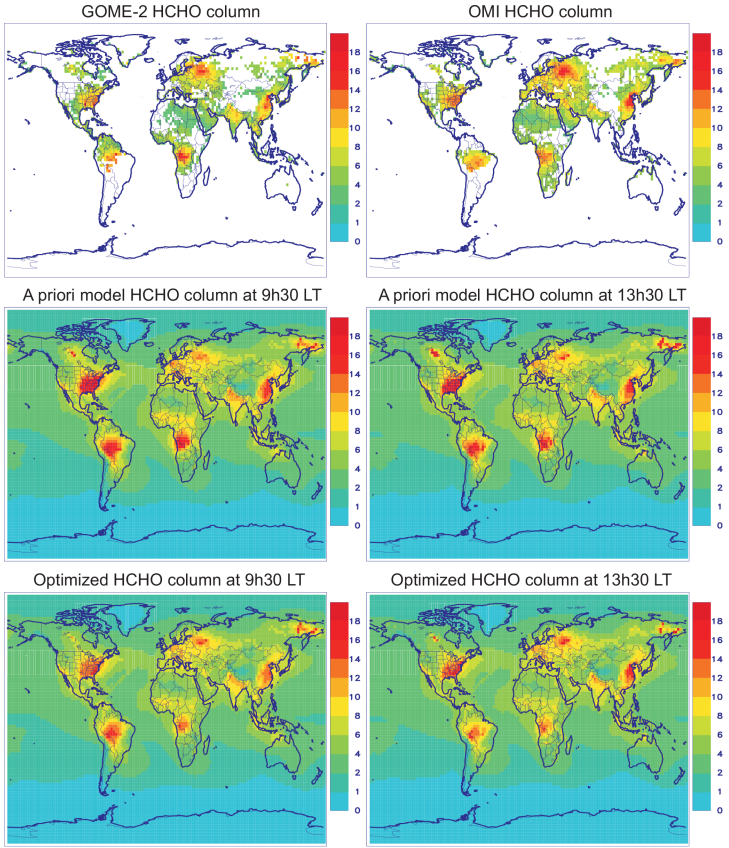

Figure 6. Observed (upper panels) HCHO columns by GOME-2 and OMI instruments in July 2010. Simulated HCHO columns using IMAGESv2 CTM at the overpass times of GOME-2 and OMI (middle panels), and optimized modelled columns derived from the inversions using GOME-2 data (left) and OMI columns (right). The columns are expressed in 10^{15} molec cm^{-2}.

ACPD
15, 12007–12067, 2015

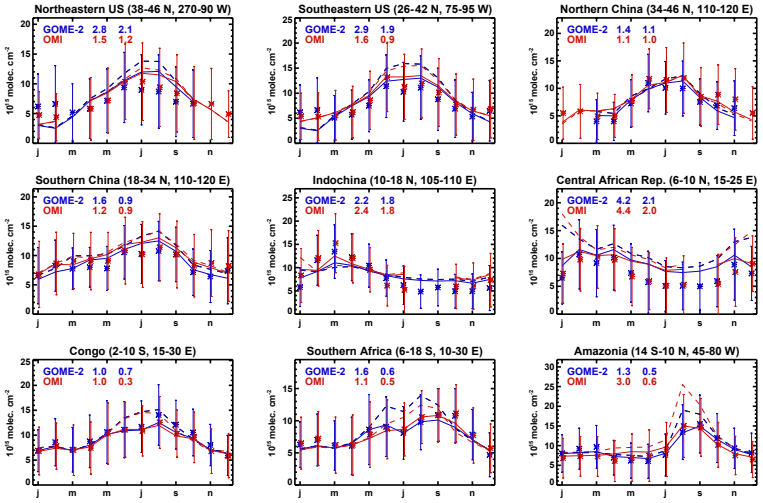

Figure 7. Monthly averages of observed GOME-2 (blue asterisks) and OMI (red asterisks) HCHO columns and modelled columns over nine selected regions. Dashed and solid lines correspond to a priori and optimized model columns, respectively, calculated at 09:30 LT (in blue) and at 13:30 LT (in red). The units are 10^{15} molec cm^{-2}. The mean absolute deviation between the a priori (left) and optimized (right) modelled and the observed columns is given inset each panel (in blue for GOME-2, in red for OMI). Error bars (blue for GOME-2, red for OMI) represent the retrieval error provided for each dataset.

ACPD
15, 12007–12067, 2015

Hydrocarbon emissions derived from GOME-2 and OMI HCHO columns

T. Stavrakou et al.

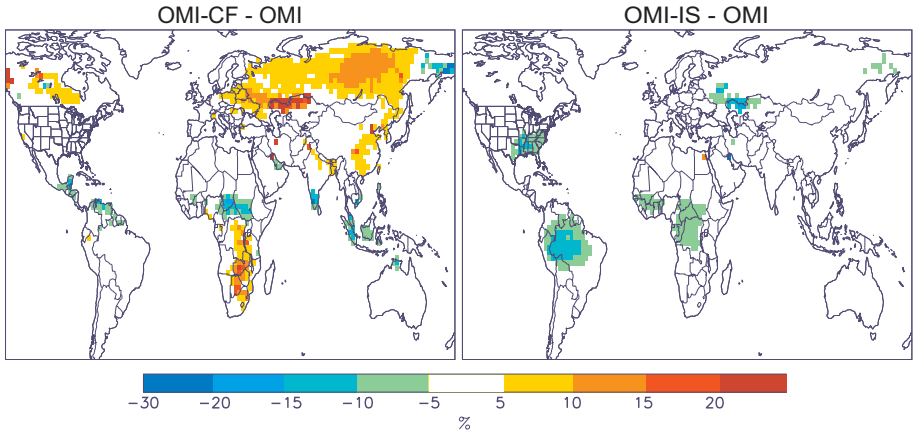

Figure 8. Percentage difference of the total VOC emissions inferred by the sensitivity inversions (OMI-CF, left panel and OMI-IS, right panel) and the standard OMI inversion for the month of July (see Table 2).

ACPD
15, 12007–12067, 2015

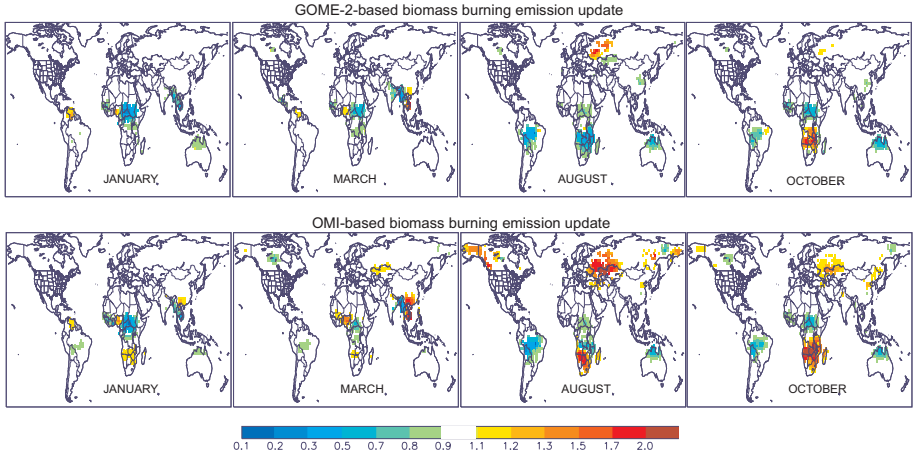

Figure 9. Ratios of optimized to a priori pyrogenic VOC fluxes derived by source inversion of HCHO columns from GOME-2 (upper panels) and OMI (lower panels) in January, March, August and October 2010. Ratio values comprised between 0.9 and 1.1 are not shown for clarity.

ACPD
15, 12007–12067, 2015

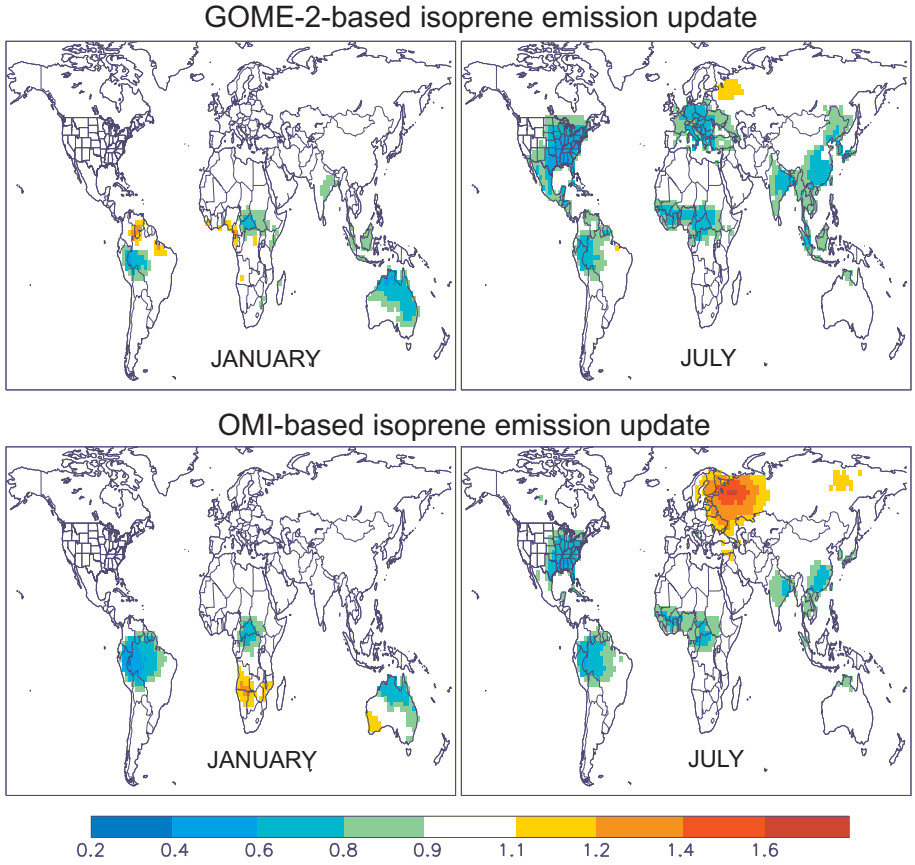

Figure 10. Same as Fig. 9, but for isoprene emissions in January and July.

ACPD
15, 12007–12067, 2015

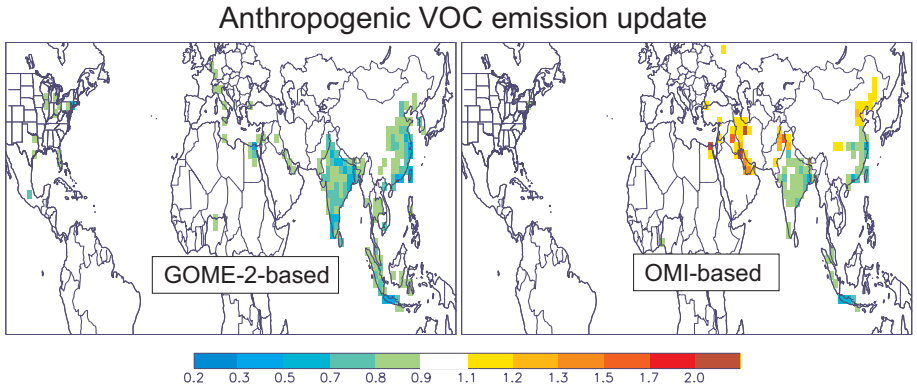

Figure 11. Same as Fig. 9, but for annual anthropogenic VOC fluxes.

ACPD
15, 12007–12067, 2015

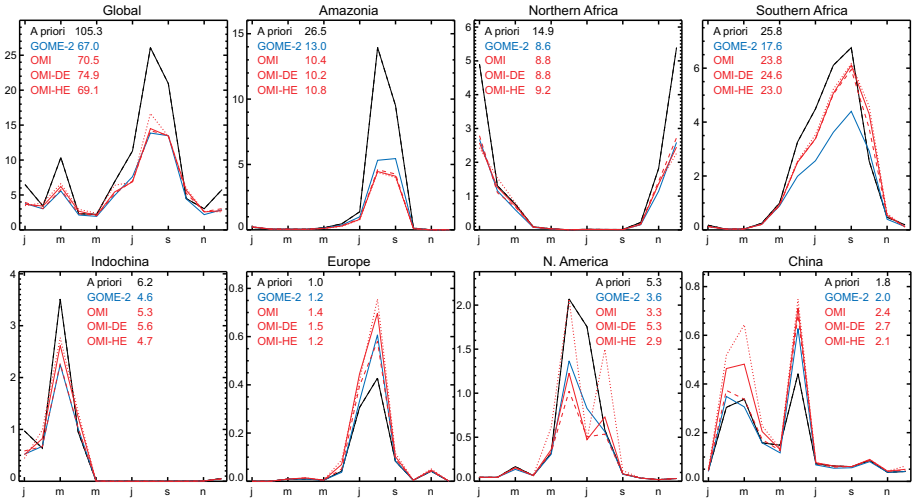

Figure 12. Monthly variation of a priori and top-down biomass burning VOC fluxes for Amazonia (14° S–10° N, 45–80° W), Africa north and south of the equator, Indochina (6–22° N, 97.5–110° E), Europe (including European Russia), N. America (US and Canada), China, and worldwide, expressed in Tg VOC. Solid lines are used for the a priori emissions (black), updated emissions inferred from GOME-2 (blue) and OMI (red) observations. Dotted and dashed red lines are used for the results of the sensitivity studies OMI-DE, and OMI-HE (Table 2), respectively. For each inversion annual fluxes for 2010 (in Tg VOC) are given inside the panels.

ACPD
15, 12007–12067, 2015

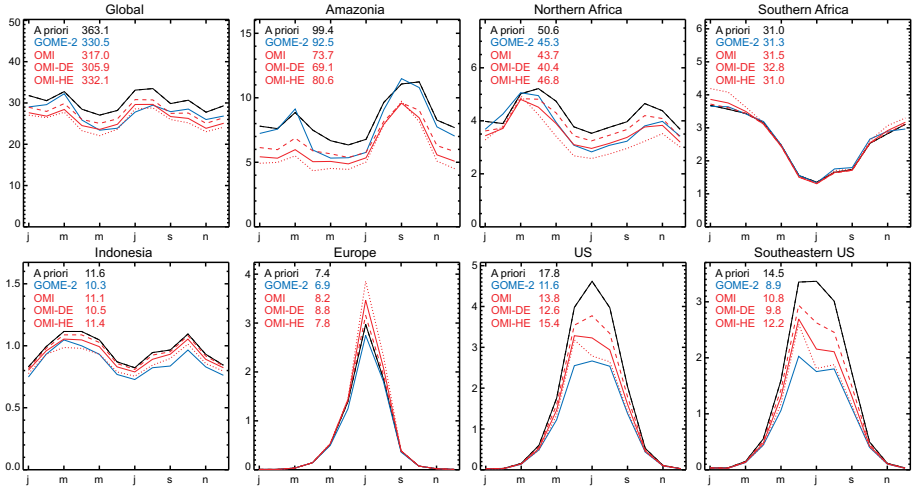

Figure 13. Monthly variation of a priori and satellite-derived isoprene fluxes for Amazonia, Northern and Southern Africa, Europe, N. America (defined as in Fig. 12), Indonesia (10° S–6° N, 95–142.5° E), and Southeastern US (25–38° N, 60–100° W). The color and line code is the same as in Fig. 12. Units are Tg of isoprene per month. Annual isoprene fluxes per region are given in each panel.

ACPD
15, 12007–12067, 2015

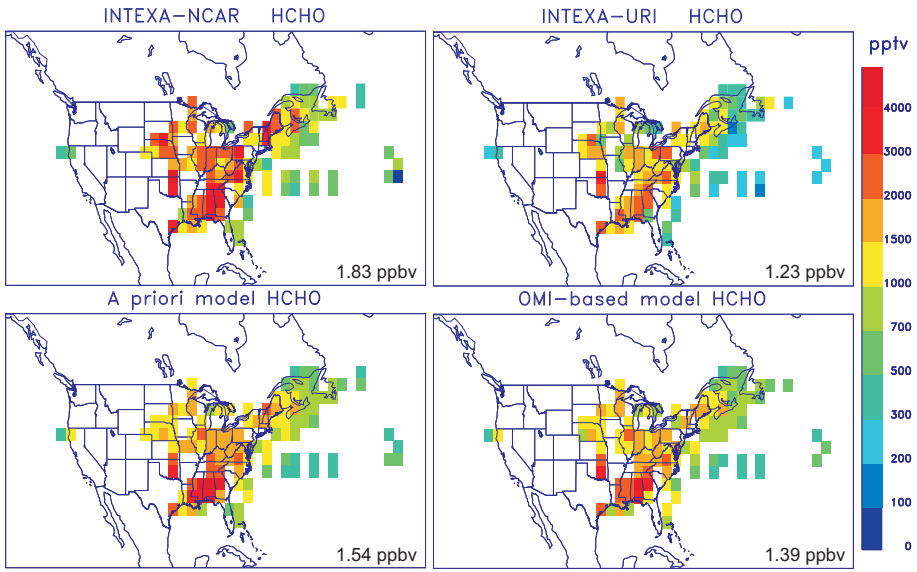

Figure 14. Comparison between HCHO measurements from the INTEX-A campaign and model concentrations sampled at the measurement times and locations from the a priori simulation and from the OMI-based inversion averaged between the surface and 2 km. The HCHO data are reported from two different instruments, from the National Center for Atmospheric Research (NCAR) and from the University of Rhode Island (URI). The observed and modelled mean HCHO concentrations over the flight domain and altitude range are given inside each panel.

ACPD
15, 12007–12067, 2015

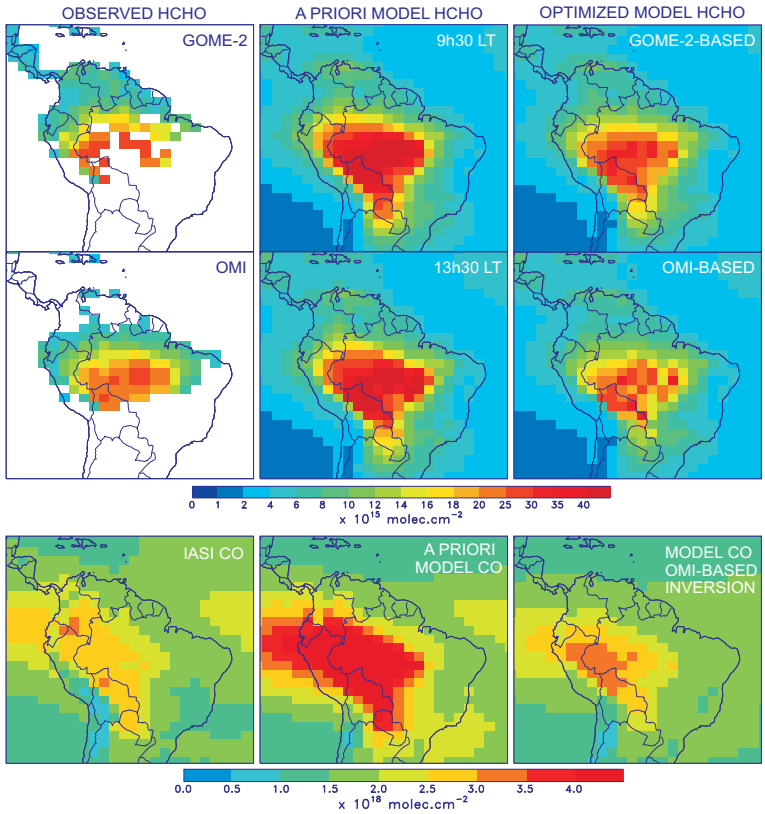

Figure 15. Observed, a priori and a posteriori model HCHO columns derived from GOME-2 (upper) and OMI (middle) inversions in Amazonia in March 2010. For the same month, observed CO columns by IASI, a priori model CO columns and CO columns from the OMI-based inversion are shown in the bottom panels. CO results from the GOME-2 inversion are very similar to those obtained from OMI and are therefore not shown here.

ACPD
15, 12007–12067, 2015

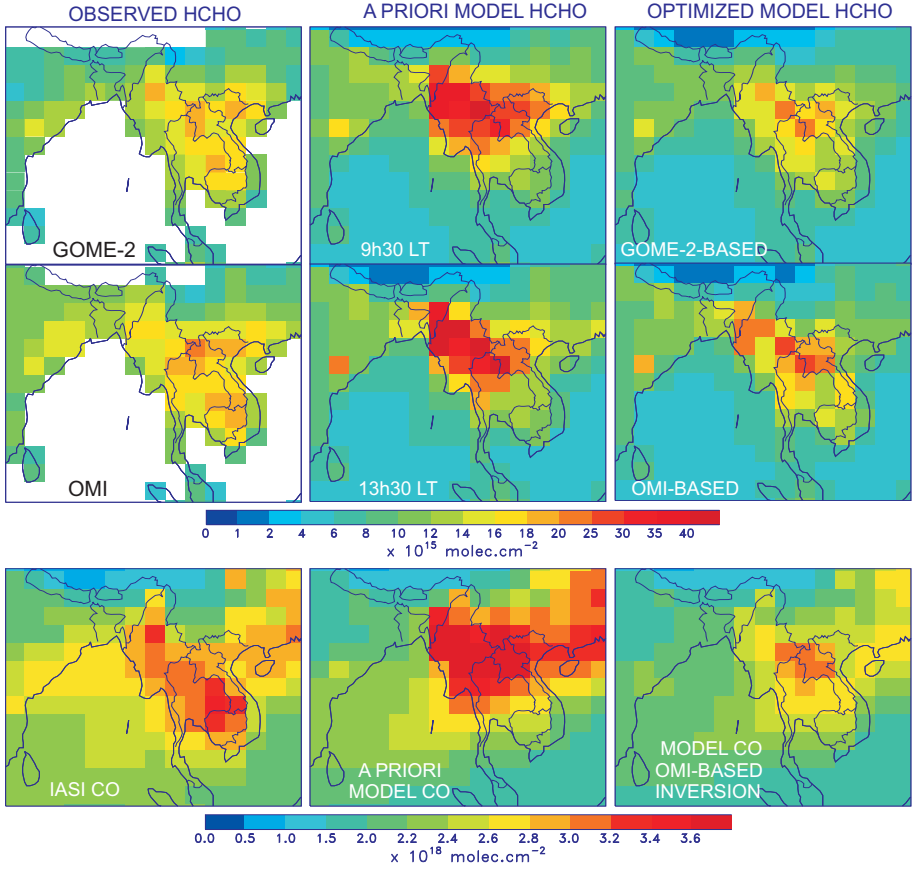

Figure 16. Same as Fig. 15 for the Indochinese Peninsula in March 2010.

ACPD
15, 12007–12067, 2015